# Internal Wave Attractors and Spectra of Zeroth-order Pseudo-differential Operators

by

**Javier A. Almonacid Paredes**

Mathematical Civil Engineer, Universidad de Concepcion, 2017
B.Sc., Universidad de Concepcion, 2015

Thesis Submitted in Partial Fulfillment of the
Requirements for the Degree of
Master of Science

in the
Department of Mathematics
Faculty of Science


**SIMON FRASER UNIVERSITY**
**Summer 2020**

# Declaration of Committee

| | |
|---|---|
| **Name:** | **Javier A. Almonacid Paredes** |
| **Degree:** | **Master of Science (Mathematics)** |
| **Thesis title:** | **Internal Wave Attractors and Spectra of Zeroth-order Pseudo-differential Operators** |
| **Committee:** | **Chair:** Stephen Choi<br>Professor, Mathematics |
| | **Nilima Nigam**<br>Senior Supervisor<br>Professor, Mathematics |
| | **Weiran Sun**<br>Supervisor<br>Associate Professor, Mathematics |
| | **Razvan Fetecau**<br>Internal Examiner<br>Professor, Mathematics |

# Abstract

The propagation of internal gravity waves in stratified media (such as those found in ocean basins and lakes) leads to the development of geometrical patterns called "attractors". These structures accumulate much of the wave energy and make the fluid flow highly singular. Microlocal analysts have recently related this behaviour to the spectral properties of an underlying nonlocal zeroth-order pseudo-differential operator that characterizes the dynamics of this problem. In this work, we analyze this phenomenon from a numerical analysis perspective. First, we propose a high-order pseudo-spectral method to solve the evolution problem, whose long-term behaviour is known to be non-square-integrable. Then, we use similar tools to discretize the corresponding eigenvalue problem. Since the eigenvalues are embedded in a continuous spectrum, their computation is based on viscous approximations. Finally, we explore the effect that the embedded eigenmodes have in the long-term evolution of the system.

**Keywords:** internal waves, pseudo-differential operators, pseudo-spectral methods, embedded eigenvalues, hyperbolic equations

# Table of Contents

# List of Tables

# List of Figures

# Chapter 1

# Introduction

Numerical analysis and scientific computing provide us with tools to probe the behaviour of complex physical models, aiding and augmenting more analytical approaches. The work in this thesis is intended to provide a computational study on the singular character of the flow of a class of zeroth-order pseudo-differential operators, in which their spectral properties play a crucial role. In particular, it concerns an abstract, highly simplified partial differential equation (PDE), which is motivated by the propagation of internal gravity waves in a stratified medium—a phenomenon whose study has been of interest by physicists and oceanographers.

## 1.1 Internal gravity waves

Gravity waves are present in the atmosphere, ocean basins and lakes. They are caused by the effect of a restoring force (in this case, gravity) that tends to bring back the fluid to its equilibrium state. Particularly in the ocean, two types of gravity waves can be found: surface waves and internal waves. The former can be easily seen since they form at the free surface of a body of fluid, while the latter propagate within the fluid. Internal waves are of upmost importance. Their role in ocean circulation is fundamental for the redistribution of momentum and energy, as well as for the movement of phytoplankton into the sunlit layer of the upper ocean, where photosynthesis occurs (cf. [19]).

Whether it is in the atmosphere or the ocean, their generation follows the same principle. In most of the cases, these waves appear when a parcel of stratified fluid (air or saline water) interacts with some topography. A fluid is said to be stratified when its density varies in the direction of the gravity force. Temperature differences in the atmosphere, and salinity variations in the oceans are a main source of stratification.

This work is motivated by a model of the propagation of internal waves in oceans, and the role that topography plays in the dynamics. In the next section we focus entirely on the derivation of the model.

### 1.1.1 Equations of motion for a continuously-stratified fluid

larger than the Coriolis frequency, the system of equations describing the motion of this fluid takes the form (according to [7]):A usual simplification while modelling the propagation of internal waves in oceans is to consider a stably-stratified non-rotating fluid, where the density $\rho$ increases with depth and depends only on the vertical direction $x_3$. Assuming that the wave motion is inviscid, that the amplitudes are small (so that nonlinear terms can be neglected from the fluid equations), and that the frequency of motion is

$$\begin{aligned} \frac{\partial \mathbf{u}}{\partial t} &= -\frac{1}{\rho_0}\nabla \Pi - \frac{\rho g}{\rho_0}\mathbf{e}_3, \\ \frac{\partial \rho}{\partial t} + \mathbf{u}\cdot\nabla\rho &= 0, \\ \nabla\cdot\mathbf{u} &= 0, \end{aligned} \tag{1.1}$$

where $\mathbf{u} = \mathbf{u}(x,t)$ (with $\mathbf{u} = (u_1, u_2, u_3)$ and $x = (x_1, x_2, x_3)$) is the fluid velocity, $\Pi$ is the pressure, $\rho_0$ is a (constant) reference density, $g$ is the gravitational acceleration and $\mathbf{e}_3$ is the unit vector in the $x_3$-direction. The flow can be thought as superimposed on a "background" state in which the density $\overline{\rho}(x_3)$ and $\overline{\Pi}(x_3)$ are in hydrostatic balance, that is:

$$0 = -\frac{1}{\rho_0}\frac{d\overline{\Pi}}{dx_3} - \frac{\overline{\rho} g}{\rho_0}. \tag{1.2}$$

Notice that $\overline{\rho}$ is allowed to vary along the vertical axis, whereas the reference density $\rho_0$ is constant throughout the domain. Once the fluid leaves the hydrostatic equilibrium, the density and pressure would evolve as:

$$\rho(x,t) = \overline{\rho}(x_3) + \rho'(x,t), \quad \Pi(x,t) = \overline{\Pi}(x_3) + \Pi'(x,t), \tag{1.3}$$

where the perturbed quantities $\rho'$ and $\Pi'$ are assumed to be small. In this way, replacing these quantities into (1.1), neglecting convective terms (recall that the amplitudes of the motions are assumed to be small as well), and using (1.2), the following equations can be obtained for the perturbations:

$$\frac{\partial \mathbf{u}}{\partial t} = -\frac{1}{\rho_0}\nabla \Pi' - \frac{\rho' g}{\rho_0}\mathbf{e}_3, \tag{1.4a}$$

$$\frac{\partial \rho'}{\partial t} = \frac{N^2 \rho_0}{g} u_3, \tag{1.4b}$$

$$\nabla\cdot\mathbf{u} = 0, \tag{1.4c}$$

where $N = N(x_3)$ is the Brunt-Väisälä frequency (or buoyancy frequency), defined as

$$N^2 := -\frac{g}{\rho_0}\frac{d\overline{\rho}}{dx_3}. \tag{1.5}$$

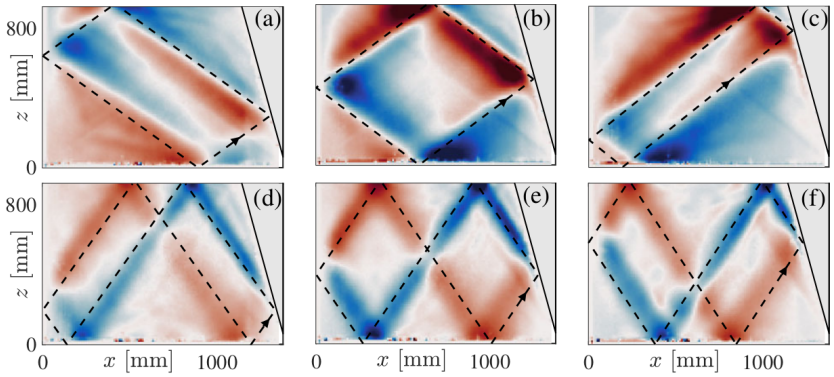


Figure 1.1: Velocity field and spatial patterns obtained after an initial impulsive kick coming from the wall on the left. Since multiple frequencies are excited at the same time, each one of the figures can be obtained by filtering the velocity field at select frequencies. Reprinted figure with permission from [13]. Copyright (2020) by the American Physical Society.

### 1.1.2 The role of topography

In domains with topography, the propagation of internal waves leads to a fluid velocity field that is highly singular. Moreover, the wave energy concentrates along geometric patterns known as *attractors*. Within the physics community, these structures have been studied at different levels: theoretically (e.g. [25, 32]), numerically (e.g. [5, 20]) and experimentally, both in two-dimensions (e.g. [22, 29]) and three-dimensions (e.g. [14, 34]). In particular, Maas et al. [29] observed using particle image velocimetry (PIV) that, in a thin channel with a trapezoidal longitudinal cross section (which can be seen as a two-dimensional trapezium) with a sloping boundary (which plays the role of the topography of the ocean basin) filled with an affine-stratified fluid, the particles move primarily within bands of finite width (due to the balance of focusing and dissipation of the waves) in which exchange of momentum and energy occurs. Since this setting has become a benchmark in experiments, we take recent result [13] as an example to show these attractors (see Figure 1.1).

## 1.2 A pseudo-differential approach

When the fluid variables are defined on a bounded domain, a common approach in Computational Fluid Dynamics is to solve the set of equations (1.4) (subject to appropriate boundary conditions) using numerical techniques such as finite difference or finite volume methods. However, if the domain is "simple", these equations can be further simplified. Indeed, taking divergence $\nabla\cdot$ in both sides of (1.4a), and using the equation for conservation of mass (1.4c), yields the pressure-Poisson equation (assuming $\rho_0$ is constant):

$$-\Delta\Pi' = g\partial_{x_3}\rho', \quad \partial_{x_j} \equiv \frac{\partial}{\partial x_j}. \tag{1.6}$$

Assuming that the domain is periodic in the $x_1$, $x_2$ and $x_3$ dimensions, the Laplacian operator $-\Delta := -\partial_{x_1}^2 - \partial_{x_2}^2 - \partial_{x_3}^2$ admits an inverse $(-\Delta)^{-1}$ (modulo constants), and hence it is possible to write

$$\Pi' = g(-\Delta)^{-1}\partial_{x_3}\rho'. \tag{1.7}$$

Replacing this expression for $\Pi'$ into (1.4a), and denoting by $\mathbf{u}_H := (u_1, u_2)$ the horizontal component of the velocity field, yields

$$\partial_t \mathbf{u}_H = -\frac{g}{\rho_0}\Big(\nabla_H(-\Delta)^{-1}\partial_{x_3}\Big)\rho', \tag{1.8a}$$

$$\partial_t u_3 = -\frac{g}{\rho_0}\Big(I + \partial_{x_3}^2(-\Delta)^{-1}\Big)\rho', \tag{1.8b}$$

$$\partial_t \rho' = -\frac{d\overline{\rho}}{dx_3}u_3, \tag{1.8c}$$

where $I$ is the identity operator and $\nabla_H := (\partial_{x_1}, \partial_{x_2})$ (the subscript $H$ will denote quantities in their horizontal components $x_1$ and $x_2$). Operators such as $\nabla_H(-\Delta)^{-1}\partial_{x_3}$ and $I + \partial_{x_3}^2(-\Delta)^{-1}$ are known as *pseudo-differential operators*, and they can be easily characterized as follows: if $\widehat{v} \equiv \mathcal{F}(v)$ denotes the Fourier transform of a smooth function $v$, then

$$\mathcal{F}\Big\{\partial_{x_1}(-\Delta)^{-1}\partial_{x_3}v\Big\}(\xi) = -\xi_1\xi_3|\xi|^{-2}\widehat{v}(\xi), \tag{1.9a}$$

$$\mathcal{F}\Big\{\partial_{x_2}(-\Delta)^{-1}\partial_{x_3}v\Big\}(\xi) = -\xi_2\xi_3|\xi|^{-2}\widehat{v}(\xi), \tag{1.9b}$$

$$\mathcal{F}\Big\{\partial_{x_3}^2(-\Delta)^{-1}v\Big\}(\xi) = -\xi_3^2|\xi|^{-2}\widehat{v}(\xi), \tag{1.9c}$$

where $\xi = (\xi_1, \xi_2, \xi_3) \in \mathbb{R}^3$ and $|\xi|$ denotes the Euclidean norm of $\xi$. In general, a smooth function $a = a(x, \xi)$ on $\mathbb{R}^n \times \mathbb{R}^n$ such that for all multi-indices $\alpha$ and $\beta$ there exists a positive constant $C_{\alpha,\beta}$ for which

$$|\partial_\xi^\alpha \partial_x^\beta a(x, \xi)| \leq C_{\alpha,\beta}(1 + |\xi|)^{m-|\alpha|} \quad \forall\, x, \xi \in \mathbb{R}^n,$$

is called a *symbol of order* $m$. This function can induce an operator $a(x, D)$ called *$m$-th order pseudo-differential operator*, which acts on rapidly decaying functions, and it is defined formally as

$$a(x, D)u(x) = \frac{1}{(2\pi)^n}\int_{\mathbb{R}^n} e^{ix\cdot\xi}a(x, \xi)\widehat{u}(\xi)\, d\xi.$$

For example, the function $a(\xi) := -\xi_1\xi_3|\xi|^{-2}$ in (1.9a) is a symbol of order 0 that defines the zeroth-order pseudo-differential operator

$$a(D) = -D_{x_1}D_{x_3}(D_{x_1}^2 + D_{x_2}^2 + D_{x_3}^2)^{-1}, \quad D_{x_j} := -i\partial_{x_j}$$

with $i := \sqrt{-1}$.

Going back to the original problem, taking the Fourier transform of the system (1.8) and assuming that the stratification is affine (so that $\frac{d\overline{\rho}}{dx_3}$ is constant) yields:

$$\partial_t \begin{pmatrix} \widehat{\rho'} \\ \widehat{u_3} \end{pmatrix} = \begin{bmatrix} 0 & -\frac{d\overline{\rho}}{dx_3} \\ -\frac{g}{\rho_0}\left(1 - \frac{\xi_3^2}{|\xi|^2}\right) & 0 \end{bmatrix} \begin{pmatrix} \widehat{\rho'} \\ \widehat{u_3} \end{pmatrix}. \tag{1.10}$$

The solution to this system is a sum of plane waves $e^{i(\xi\cdot x - \omega t)}$, with dispersion relation depending on the buoyancy frequency $N$ (cf. (1.5)):

$$\omega := \pm N \frac{|\xi_H|}{|\xi|}.$$

Moreover, this system can be written as

$$\partial_t \widehat{\mathbf{v}} + \mathbf{M}\widehat{\mathbf{v}} = 0,$$

where $\widehat{\mathbf{v}} = \left(\widehat{\rho'}, \widehat{u_3}\right)^T$ ($T$ denotes the transpose vector). Since the matrix $\mathbf{M}$ can be viewed as

$$\mathbf{M} := \begin{bmatrix} 0 & -\frac{d\overline{\rho}}{dx_3} \\ -\frac{g}{\rho_0}\left(1 - \frac{\xi_3^2}{|\xi|^2}\right) & 0 \end{bmatrix} = \begin{bmatrix} \mathbf{e}_+ & \mathbf{e}_- \end{bmatrix} \begin{bmatrix} \lambda_+ & 0 \\ 0 & \lambda_- \end{bmatrix} \begin{bmatrix} \mathbf{e}_+ & \mathbf{e}_- \end{bmatrix}^{-1},$$

where

$$\lambda_\pm = \pm iN\frac{|\xi_H|}{|\xi|}, \quad \mathbf{e}_\pm = \left(\pm i\sqrt{-\frac{d\overline{\rho}}{dx_3}\frac{\rho_0}{g}}\,\frac{|\xi|}{|\xi_H|}\ ,\ 1\right)^T,$$

upon formal diagonalization $\widehat{\mathbf{v}} = \widehat{u_+}\mathbf{e}_+ + \widehat{u_-}\mathbf{e}_-$, the system (1.10) reduces to find $\widehat{u_\pm}$ satisfying

$$i\partial_t \widehat{u_\pm} \mp N\frac{|\xi_H|}{|\xi|}\widehat{u_\pm} = 0.$$

That is, $u_\pm$ satisfy the pair of hyperbolic equations

$$i\partial_t u_\pm \mp \mathcal{P}(D)u_\pm = 0, \tag{1.11}$$

where $\mathcal{P}(D)$ is the zeroth-order pseudo-differential

$$\mathcal{P}(D) = N\,\frac{|D_H|}{|D|}, \quad D := (D_{x_1}, D_{x_2}, D_{x_3}).$$

It can be readily seen that the symbol of $\mathcal{P}$ is singular at $\xi = 0$. In addition, it is worth noting that zeroth-order operators such as $\mathcal{P}$ can act not only on rapidly decaying functions but also on square-integrable functions (cf. [23, Theorem 18.1.11]).

The theory of pseudo-differential operators emerges as a powerful tool to analyze linear PDEs such as (1.11) (see, for instance, [23]). Therefore, it is expected that the analysis of the operator $\mathcal{P}$ will lead to some information on the generation and propagation of internal waves.

## 1.3 Microlocal analysis of internal waves

When a container of fluid is vibrated, its response can be described in terms of the eigenmodes (eigenfunctions) of the system. These manifest as large-scale standing waves, which in many cases are visible to the naked-eye. In this scenario, the eigenmodes are assumed to be smooth quantities that completely describe the system, and therefore, the solution to the modelling PDE is expected to be smooth. The eigenfrequencies (eigenvalues) thus form a countable set. This is the case when for instance, the boundary of the container is smooth and the flow inside can be modelled by the equation

$$\partial_t \mathbf{u} - \Delta \mathbf{u} = \mathbf{f},$$

where $\mathbf{f}$ is a smooth source term and $\Delta$ is the standard Laplacian. In this case, the eigenfunctions of $-\Delta$ are smooth, they form a basis of the space of square-integrable functions, and therefore the solution $\mathbf{u}$ can be exclusively written in terms of these eigenfunctions.

Internal gravity waves in uniformly stratified fluids comprise a different scenario. Here, the flow is singular in the spatial variables, and thus cannot completely be described by smooth eigenmodes (if any). Moreover, Maas et al. [29] report that "internal wave attractors, rather than eigenmodes" determine the response to the system, suggesting that there is a different mechanism that drives the response to these kind of systems. The fact that these attractors are present for a wide range of frequencies (cf. [28]) suggests the presence of a *continuous spectrum* and a lack of eigenmodes.

In the past two decades, many studies have been performed in the physics community to better comprehend these issues (see, for example, the references at the beginning of Section 1.1.2). A mathematical explanation of this phenomenon has only been recently provided by Colin de Verdière & Saint-Raymond [9]. In this work, by means of microlocal analysis (i.e., the connection between spectral theory and classical dynamics), the authors are able to confirm many of the findings by Maas et al. [28, 29]. This relationship had been explored in the past for related problems, such as the work by Ralston [35] for inertial waves in some specific two-dimensional geometries. To better understand the dynamical assumptions made by [9], a brief review on Hamiltonian flows and Morse theory is needed.

### 1.3.1 Hamiltonian and Morse-Smale flows

Hamiltonian flows have their origin in Hamiltonian mechanics. They are generated by the namesake vector field $H_f$, which for a smooth function $f$ on $\mathbb{R}^n \times \mathbb{R}^n$ is given by

$$H_f = \sum_{j=1}^{n} \frac{\partial f}{\partial \xi_j}\frac{\partial}{\partial x_j} - \frac{\partial f}{\partial x_j}\frac{\partial}{\partial \xi_j}.$$

Then, the Hamilton ordinary differential equations (ODEs) become:

$$\frac{dx}{ds} = \frac{\partial H_f}{\partial \xi}, \quad \frac{d\xi}{ds} = -\frac{\partial H_f}{\partial x}.$$

On the other hand, the characterization of Morse-Smale flows dates from the work by Smale [40], and it requires a handful of previous concepts for their understanding (see Appendix A and the references therein for more details). In a summarized way, Morse-Smale systems are dynamical systems whose non-wandering set consists of finitely many hyperbolic equilibrium points and hyperbolic periodic orbits, and whose stable and unstable manifolds satisfy a transversality condition.

These flows are structurally stable and have good stability properties (cf. [31]). They appear as a generalization of gradient flows by a Morse function. First, a smooth function $f$ is said to be *Morse* if all its critical points are isolated and non-degenerate (that is, the determinant of the Hessian matrix at any of these points is nonzero). Let $M$ be a smooth compact manifold without boundary, equipped with a smooth Riemannian metric. Then, $V(x) = -\nabla f(x)$ defines a vector field on $M$. Fix a point $z \in \mathbb{R}^n$ and solve the system of ODEs:

$$\frac{dw}{dt} = V(w), \quad t \in \mathbb{R}, \qquad w(0) = z.$$

The flow map $f^t$, $t \in \mathbb{R}$, where $f^t(z) := w(t; z)$, can be shown to be Morse-Smale whenever $f$ is Morse and the unstable and stable manifolds intersect transversally (cf. [39]).

### 1.3.2 Regularity of the flow and existence of eigenmodes

The study by Colin de Verdière & Saint-Raymond [9]–the first of its type for internal waves– is based on the analysis of equations of the form (1.11). More precisely, they consider the equation

$$iu_t - Pu = fe^{-i\omega_0 t} \tag{1.12}$$

on a two-dimensional torus $\mathbb{T}^2$, where $fe^{-i\omega_0 t}$ is a periodic smooth forcing and $P$ is a bounded, self-adjoint, zeroth-order pseudo-differential operator satisfying some hyperbolic dynamical assumptions, which would be later relaxed (to a certain degree) by Colin de Verdière [8] and Dyatlov & Zworski [17]. In particular, the study of (1.12) in [8, 9, 17] views the evolution of (1.12) as the flow on an energy manifold generated by the Hamiltonian

vector field $H_p$ associated to the principal symbol $p$ of $P$, which is assumed to be Morse-Smale with no fixed points.

The main results in [8, 9, 17] are essentially the same (but obtained with different methods). First, they confirm that internal-wave attractors form when $P$ has some continuous spectrum. More precisely, the spectrum of $P$ in a neighbourhood of 0 is shown to be absolutely continuous with possibly finitely many embedded eigenvalues. The eigenfunctions associated to the embedded eigenvalues are analytic (cf. [44]). Then, they prove that the long-term evolution of the flow (where the attractors are fully developed) is not a square-integrable function. Indeed, as $t \to \infty$, the solution of (1.12) is a distribution living in Sobolev spaces $\mathrm{H}^s$ of negative order. We note these works are very recent (the oldest one [9] first appeared in 2018).

### 1.3.3 Viscous limit

It is evident that the computation of the embedded eigenmodes of $P$ is a challenging problem. Works such as the one by Rieutord et al. [36] suggest that a way to overcome this difficulty is to consider a regularized problem which introduces a small viscosity $\nu > 0$. The interest is then to compute the eigenmodes of the viscous operator $P + i\nu\Delta$ (with $-\Delta$ the standard Laplacian) for very low viscosities. While this makes sense from a physical point of view, the mathematical picture is not too straightforward.

On the one hand, the operator $P$ is of zeroth-order with a combination of continuous spectrum and embedded eigenvalues. On the other hand, $P+i\nu\Delta$ is a second-order operator with a purely discrete spectrum. Hence, the eigenvalues of $P + i\nu\Delta$ may not necessarily converge to those of $P$ as $\nu \to 0^+$. However, in some other contexts, there is mathematical evidence that this limit makes sense for some elements of the spectrum of $P$ (see, for instance, the viscous approximation of Pollicot-Ruelle resonances by Dyatlov & Zworski [15]). An answer to this problem (for the specific $P$ under study) was given by Galkowski & Zworski [18]. There, it is shown that the limit set of eigenvalues of $P+i\nu\Delta$ as $\nu \to 0^+$ gives a set of resonances that includes some of the embedded eigenvalues of $P$ in a neighbourhood of 0. This work also sheds some light on the regularity of the viscous eigenmodes, and how they might not be described as functions.

## 1.4 Goals and outline

The setting provided by Colin de Verdière & Saint-Raymond [9] and Dyatlov & Zworski [17] opens the door to new ways of analyzing this kind of problems, such as using tools from numerical analysis. To this date, no provably convergent numerical methods have been provided for the evolution problem (1.12) or for its associated eigenvalue problem.

According to the above, we focus in this work on the development of numerical tools to approximate the solution to equations of the form (1.12) in the 2-torus and the eigenvalue

problem

$$(P + i\nu\Delta)u = \lambda u, \quad \nu > 0, \tag{1.13}$$

where $P = P(x, D)$ is the zeroth-order pseudo-differential operator

$$P(x, D) = (I + D_{x_1}^2 + D_{x_2}^2)^{-1/2} D_{x_2} - r\beta(x),$$

where $r$ is a positive number and $\beta$ is a smooth function (the form of this operator can be considered as a generalization of the examples considered in [17]). Moreover, given the absence of boundaries, different versions of the term $r\beta$ will lead to attractors with different shapes. In general, the distributional character of the evolution and the non-square-integrability for long times, as well as the embedding of the eigenvalues in the continuous spectrum will be the main challenges in this computational study.

Since the problems are posed on a periodic domain, we discretize the equations using a pseudo-spectral approach, which has proven to be a powerful tool to solve nonlocal problems in periodic domains (see, for instance, [2, 24, 43]). We then use these tools to explore the effect that the embedded eigenmodes have on the long-term evolution of the flow, for which we resort to the viscous approximation described by [18] (see Section 1.3.3). Some of these results will be explained using the microlocal analysis ideas from [9, 17]. In general, emphasis will be put into analyzing the results in frequency space, since this will give us insight into how smooth a function (or distribution) is (see, for instance, [6, 38]).

This thesis is organized as follows. In Chapter 2 we formalize the description of the considered pseudo-differential operator and the evolution problem. Here, we provide evidence of accuracy and convergence by performing standard error tests and contrasting these results to those in [9, 17]. Then, in Chapter 3, we focus on the eigenvalue problem (1.13), its discretization and the main computational challenges that arise. In Chapter 4, we use the methods developed in the previous chapters to explore more in depth the eigenvalue problem, and the relationship between the embedded eigenmodes and the long-term dynamics of the problem. Finally, in Chapter 5 we draw some conclusions on the obtained results and provide some ideas for future work.

# Chapter 2

# The Evolution Problem

In this chapter, we formally introduce the evolution problem to be studied. First, since the pseudo-differential operator to be considered can be better understood by means of the Fourier transform, we fix notation and recall important definitions from [37]. Then, we present convergent discretizations to approximate the solutions to this problem, where we will see how the presence of attractors make computations challenging.

Throughout this work, we shall denote $|\cdot|$ as either the modulus of a complex number or the Euclidean norm of a point in $\mathbb{R}^2$, and the Japanese bracket as $\langle\, \xi \,\rangle := (1 + |\xi|^2)^{1/2}$ for any $\xi \in \mathbb{R}^2$.

## 2.1 Preliminaries

**Definition 2.1** (Schwartz space $\mathcal{S}(\mathbb{Z}^2)$)**.** *We denote by $\mathcal{S}(\mathbb{Z}^2)$ the topological space of rapidly decaying functions $\mathbb{Z}^2 \to \mathbb{C}$ such that $\varphi \in \mathcal{S}(\mathbb{Z}^2)$ if and only if for any $M < \infty$, there exists a constant $C_{\varphi,M}$ such that*

$$|\varphi(\xi)| \leq C_{\varphi,M} \langle\, \xi \,\rangle^{-M} \quad \forall\ \xi \in \mathbb{Z}^2.$$

*The topology on $\mathcal{S}(\mathbb{Z}^2)$ is induced by the seminorms $p_k$, where $k \in \mathbb{N}_0$ and*

$$p_k(\varphi) := \sup_{\xi \in \mathbb{Z}^2} \langle\, \xi \,\rangle^k |\varphi(\xi)|.$$

**Definition 2.2** (Tempered distributions $\mathcal{S}'(\mathbb{Z}^2)$)**.** *We denote by $\mathcal{S}'(\mathbb{Z}^2)$ the space of tempered distributions, consisting of continuous linear functionals on $\mathcal{S}(\mathbb{Z}^2)$. This means that $u \in \mathcal{S}'(\mathbb{Z}^2)$ if it is a functional $u : \mathcal{S}(\mathbb{Z}^2) \to \mathbb{C}$ such that:*

1. *$u$ is linear, i.e., $u(\alpha\varphi + \beta\psi) = \alpha u(\varphi) + \beta u(\psi)$ for all $\alpha, \beta \in \mathbb{C}$ and all $\varphi, \psi \in \mathcal{S}(\mathbb{Z}^2)$;*
2. *$u$ is continuous, i.e., $u(\varphi_j) \to u(\varphi)$ in $\mathbb{C}$ whenever $\varphi_j \to \varphi$ in $\mathcal{S}(\mathbb{Z}^2)$.*

*We also denote by $\langle\, \cdot, \cdot \,\rangle$ the duality pairing between $\mathcal{S}'(\mathbb{Z}^2) \times \mathcal{S}(\mathbb{Z}^2)$, so we may write $\langle\, u, \varphi \,\rangle$, instead of $u(\varphi)$, for $u \in \mathcal{S}'(\mathbb{Z}^2)$ and $\varphi \in \mathcal{S}(\mathbb{Z}^2)$.*

**Remark 2.3.** *It can be shown that the elements $u \in \mathcal{S}'(\mathbb{Z}^2)$ are of the form*

$$\varphi \mapsto \langle\, u, \varphi \,\rangle := \sum_{\xi \in \mathbb{Z}^2} u(\xi)\, \varphi(\xi),$$

*where $u : \mathbb{Z}^2 \to \mathbb{C}$ grows at most polynomially at infinity, i.e., there exists constants $M < \infty$ and $C_{u,M}$ such that*

$$|u(\xi)| \leq C_{u,M} \langle\, \xi \,\rangle^M \quad \forall\ \xi \in \mathbb{Z}^2.$$

*Therefore, the elements in $\mathcal{S}'(\mathbb{Z}^2)$ are pointwise well-defined functions on the lattice $\mathbb{Z}^2$.*

**Definition 2.4** (1-periodic functions, space $C^\infty(\mathbb{T}^2)$)**.** *A function $f : \mathbb{R}^2 \to \mathbb{C}$ is 1-periodic if $f(x + k) = f(x)$ for every $x \in \mathbb{R}^2$ and $k \in \mathbb{Z}^2$. We shall consider these functions to be defined on $\mathbb{T}^2 = \mathbb{R}^2/\mathbb{Z}^2 = \{x + \mathbb{Z}^2,\ x \in \mathbb{R}^2\}$. The space of 1-periodic $m$-times continuously differentiable functions is denoted by $C^m(\mathbb{T}^2)$, and thus we define $C^\infty(\mathbb{T}^2) := \cap_{m \geq 1} C^m(\mathbb{T}^2)$.*

**Definition 2.5** (Periodic distributions $\mathcal{D}'(\mathbb{T}^2)$)**.** *We denote by $\mathcal{D}'(\mathbb{T}^2)$ the topological space of periodic distributions, that is, the space of all continuous linear functionals $C^\infty(\mathbb{T}^2) \to \mathbb{C}$. The topology of $\mathcal{D}'(\mathbb{T}^2)$ is the weak*-topology, meaning that the convergence is defined in a pointwise way. This is, a sequence $\{v_n\}_{n \geq 1} \subset \mathcal{D}'(\mathbb{T}^2)$ converges to $v \in \mathcal{D}'(\mathbb{T}^2)$ if and only if*

$$v_n(\psi) \to v(\psi) \quad \forall\ \psi \in C^\infty(\mathbb{T}^2).$$

We are now ready to define the Fourier transform on $\mathbb{T}^2$, first on smooth functions and then on distributions.

**Definition 2.6.** *Let $\mathcal{F} : C^\infty(\mathbb{T}^2) \to \mathcal{S}(\mathbb{Z}^2)$ be the (toroidal) Fourier transform defined as*

$$(\mathcal{F} f)(\xi) \equiv \widehat{f}(\xi) := \frac{1}{2\pi} \int_{\mathbb{T}^2} f(x)\, e^{-ix\cdot\xi}\, dx. \tag{2.1}$$

*The operator $\mathcal{F}$ is a bijection, and as such, it admits an inverse $\mathcal{F}^{-1} : \mathcal{S}(\mathbb{Z}^2) \to C^\infty(\mathbb{T}^2)$ given by*

$$(\mathcal{F}^{-1} \widehat{f})(x) \equiv f(x) := \frac{1}{2\pi} \sum_{\xi \in \mathbb{Z}^2} \widehat{f}(\xi)\, e^{ix\cdot\xi}. \tag{2.2}$$

Using this inverse transform, the Fourier transform can then be uniquely extended to a mapping $\mathcal{F} : \mathcal{D}'(\mathbb{T}^2) \to \mathcal{S}'(\mathbb{Z}^2)$ by

$$\langle\, \mathcal{F} u, \varphi \,\rangle := \Big\langle\, u, \mu \circ \mathcal{F}^{-1} \varphi \,\Big\rangle \quad \forall\ \varphi \in \mathcal{S}(\mathbb{Z}^2), \tag{2.3}$$

where $u \in \mathcal{D}'(\mathbb{T}^2)$ and $\mu$ is defined by $(\mu \circ \eta)(x) := \eta(-x)$ for any smooth function $\eta$. Hereafter, we will make use of the Fourier transform defined as in (2.3), but still using formula (2.1).

Thus, we can use the Fourier transform to define derivatives of distributions. First, distributional derivatives can be defined as

$$\langle\, \partial^\alpha u, \varphi \,\rangle := \Big\langle\, u, (-1)^{|\alpha|} \partial^\alpha \varphi \,\Big\rangle$$

where $\alpha = (\alpha_1, \alpha_2) \in (\mathbb{N} \cup \{0\})^2$ is a multi-index, $|\alpha| = \alpha_1 + \alpha_2$ and $\partial^\alpha := \partial_{x_1}^{\alpha_1} \partial_{x_2}^{\alpha_2}$. Then, using (2.3), we can write for $\varphi \in C^\infty(\mathbb{T}^2)$:

$$\begin{aligned}
\langle\, \mathcal{F}(\partial^\alpha u), \varphi \,\rangle &= \Big\langle\, \partial^\alpha u, \mu \circ \mathcal{F}^{-1} \varphi \,\Big\rangle \\
&= \Big\langle\, u, (-1)^{|\alpha|} \partial^\alpha (\mu \circ \mathcal{F}^{-1} \varphi) \,\Big\rangle \\
&= \left\langle\, u, (-1)^{|\alpha|} \partial^\alpha \left( \frac{1}{2\pi} \sum_{\xi \in \mathbb{Z}^2} \widehat{\varphi}(\xi) e^{-ix\cdot\xi} \right) \right\rangle \\
&= \Big\langle\, u, (-1)^{|\alpha|} (-i\xi)^\alpha \mu \circ \mathcal{F}^{-1} \varphi \,\Big\rangle \\
&= (i\xi)^\alpha \Big\langle\, u, \mu \circ \mathcal{F}^{-1} \varphi \,\Big\rangle \\
&= \langle\, (i\xi)^\alpha \mathcal{F} u, \varphi \,\rangle,
\end{aligned}$$

and therefore

$$\partial^\alpha u(x) = \mathcal{F}^{-1}\Big( (i\xi)^\alpha\, \widehat{u}(\xi) \Big) \quad \text{in } \mathcal{D}'(\mathbb{T}^2),$$

where for any $\zeta = (\zeta_1, \zeta_2) \in \mathbb{C}^2$, we denote $\zeta^\alpha := \zeta_1^{\alpha_1} \zeta_2^{\alpha_2}$.

Among all distributions, we will be particularly interested in those that form Hilbert spaces, that is, Sobolev spaces of negative order $\mathrm{H}^s(\mathbb{T}^2)$ for $s < 0$.

**Definition 2.7.** *Let $s \in \mathbb{R}$. Then, we define the Sobolev space $\mathrm{H}^s(\mathbb{T}^2)$ by means of a weighted norm, that is*

$$\mathrm{H}^s(\mathbb{T}^2) := \left\{ f : \mathbb{T}^2 \to \mathbb{R} \quad : \quad \| f \|_s^2 := \sum_{\xi \in \mathbb{Z}^2} \langle\, \xi \,\rangle^{2s} \left| \widehat{f}(\xi) \right|^2 < \infty \right\}, \tag{2.4}$$

*where $\widehat{f}(\xi)$ are the (generalized) Fourier coefficients. In particular, $\mathrm{L}^2(\mathbb{T}^2) = \mathrm{H}^0(\mathbb{T}^2)$.*

**Remark 2.8.** *Let $s \in \mathbb{Z}$. The norm $\| \cdot \|_s$ is equivalent to the usual Sobolev norm*

$$\| f \|_s' := \left( \sum_{|\alpha| \le s} \int_{\mathbb{T}^2} |\partial^\alpha f(x)|^2 \, dx \right)^{1/2},$$

*where $\alpha = (\alpha_1, \alpha_2) \in (\mathbb{N} \cup \{0\})^2$ is a multi-index. Indeed, [37, Exercise 3.2.7] shows that for $s \in \mathbb{N} \cup \{0\}$, there exists a constant $C_s$ such that*

$$\| u \|_s \le \| u \|_s' \le C_s \| u \|_s.$$

## 2.2 The forced linear wave equation

We consider the problem of finding a complex function $u = u(x,t)$, $x = (x_1, x_2) \in \mathbb{T}^2$, $t \geq 0$ such that

$$iu_t - Pu = fe^{-i\omega_0 t} \quad \text{in } \mathbb{T}^2 \times (0,\infty), \qquad u\big|_{t=0} = 0. \tag{2.5}$$

where $f \in C^\infty(\mathbb{T}^2)$, $\omega_0 \geq 0$ is a forcing frequency, and $P$ is the zeroth-order pseudo-differential operator acting on elements of $\mathrm{L}^2(\mathbb{T}^2)$ defined by

$$P(x,D)v(x) = \langle\, D\,\rangle^{-1} D_{x_2} v(x) - r\beta(x)v(x), \quad r > 0, \tag{2.6}$$

where $D = (D_{x_1}, D_{x_2})$, $D_{x_j} := -i\partial_{x_j} = -i\frac{\partial}{\partial x_j}$ and $\beta \in C^\infty(\mathbb{T}^2)$ is a real function. Then, using the inverse Fourier transform, the Kohn-Niremberg definition (cf. [26]) of $P$ reads

$$P(x,D)v(x) = \frac{1}{2\pi} \sum_{\xi \in \mathbb{Z}^2} \left[\langle\, \xi\,\rangle^{-1} \xi_2 - r\beta(x)\right] \widehat{v}(\xi)\, e^{ix\cdot\xi}. \tag{2.7}$$

With this definition, it is easy to see that $P$ is a bounded and self-adjoint operator (with the standard $\mathrm{L}^2(\mathbb{T}^2)$ inner product). Indeed, since $|\langle\, \xi\,\rangle^{-1}\xi_2| \leq 1$ for any $\xi \in \mathbb{R}^2$, using Plancherel's identity we obtain

$$\begin{aligned}
\| Pv \|_{\mathrm{L}^2(\mathbb{T}^2)} &\leq \left\| \langle\, D\,\rangle^{-1} D_{x_2} v \right\|_{\mathrm{L}^2(\mathbb{T}^2)} + r \| \beta v \|_{\mathrm{L}^2(\mathbb{T}^2)} \\
&\leq \left( \sum_{\xi \in \mathbb{Z}^2} |\langle\, \xi\,\rangle^{-1} \xi_2 \widehat{v}(\xi)|^2 \right)^{1/2} + r \| \beta \|_{\mathrm{L}^\infty(\mathbb{T}^2)} \| v \|_{\mathrm{L}^2(\mathbb{T}^2)} \\
&\leq \left(1 + r \| \beta \|_{\mathrm{L}^\infty(\mathbb{T}^2)}\right) \| v \|_{\mathrm{L}^2(\mathbb{T}^2)} \quad \forall\ v \in \mathrm{L}^2(\mathbb{T}^2),
\end{aligned}$$

showing that $P : \mathrm{L}^2(\mathbb{T}^2) \to \mathrm{L}^2(\mathbb{T}^2)$ is bounded, and

$$\begin{aligned}
\int_{\mathbb{T}^2} Pu\, \overline{v}\, dx &= \sum_{\xi \in \mathbb{Z}^2} \langle\, \xi\,\rangle^{-1} \xi_2 \widehat{u}(\xi) \overline{\widehat{v}(\xi)} - r \int_{\mathbb{T}^2} \beta u \overline{v}\, dx \\
&= \sum_{\xi \in \mathbb{Z}^2} \widehat{u}(\xi) \overline{\langle\, \xi\,\rangle^{-1} \xi_2 \widehat{v}(\xi)} - r \int_{\mathbb{T}^2} u \overline{\beta v}\, dx \\
&= \int_{\mathbb{T}^2} u \overline{\langle\, D\,\rangle^{-1} D_{x_2} v}\, dx - r \int_{\mathbb{T}^2} u \overline{\beta v}\, dx = \int_{\mathbb{T}^2} u\, \overline{Pv}\, dx,
\end{aligned}$$

for any $u, v \in \mathrm{L}^2(\mathbb{T}^2)$.

Moreover, it can be shown that the problem (2.5) is well-posed in $C(0,T;\mathrm{L}^2(\mathbb{T}^2))$ for any $T > 0$, $f \in C^\infty(\mathbb{T}^2)$ and $\omega_0 \geq 0$ (cf. [17]). However, the solution is expected to be non-smooth for long times, with a limiting long-term behaviour that is not square-integrable. Indeed, microlocal analysis techniques can then be used to give insight into the regularity of the solution to (2.5). The following result is a consequence of [9, Theorem 3.1] and [17].

**Theorem 2.9.** *Let $f \in C^\infty(\mathbb{T}^2)$, $\omega_0$ not an eigenvalue of $P$. Then, the solution to* (2.5) *can be uniquely decomposed as*

$$u(t) = e^{-i\omega_0 t} u_\infty + b(t) + \epsilon(t), \tag{2.8}$$

*where*

1. *$u_\infty := \lim_{\varepsilon \to 0} (P - \omega_0 - i\varepsilon)^{-1} f$ belongs to $\mathrm{H}^s(\mathbb{T}^2)$ for any $s < -1/2$ and is not in $\mathrm{L}^2(\mathbb{T}^2)$ except if it vanishes,*
2. *$b$ is a bounded function with values in $\mathrm{L}^2(\mathbb{T}^2)$,*
3. *$\epsilon$ vanishes as $t \to \infty$ in the $\mathrm{H}^s(\mathbb{T}^2)$-norm, for any $s < -1/2$.*

*Moreover, the energy $\| u(t) \|_0^2$ grows linearly except if $u_\infty$ vanishes.*

While this result is stated in [9, Theorem 3.1] for a general bounded, self-adjoint, pseudo-differential operator of degree 0 that satisfies certain dynamical assumptions, the structure of the operator defined in (2.6) has been considered in [17] as a feasible choice for this problem. Furthermore, the aforementioned work also proves a similar version of Theorem 2.9, but this time using standard radial estimates (cf. [16, §E.4]).

## 2.3 Discrete setting

In this section, we present a set of tools that will be necessary for the discretization of the evolution problem (2.5). While in the continuous case, we were able to make sense of (2.5) by means of the Fourier transform, in the discrete case, we will make use of the discrete Fourier transform. Let us first consider a discretization of $\mathbb{T}^2$.

**Definition 2.10** (Mesh of $\mathbb{T}^2$, wave numbers)**.** *Let $N \geq 2$ be an even integer. We refer to the set*

$$\mathcal{T}_N := \left\{ x_j = (x_{j_1}, x_{j_2}) \in \mathbb{R}^2 \ : \ x_{j_\iota} = 2\pi j_\iota / N, \ j_\iota = -N/2, \dots, N/2 - 1 \right\}, \tag{2.9}$$

*as a mesh of $\mathbb{T}^2$ containing $N^2$ grid points. Similarly, we refer to*

$$\mathcal{W}_N := \left\{ k = (k_1, k_2) \in \mathbb{Z}^2 \ : \ k_\iota = -N/2, \dots, N/2 - 1 \right\} \tag{2.10}$$

*as the set of wave numbers, whose cardinality is also $N^2$.*

For now, let us fix some time $t > 0$ and write $u_N = u_N(\cdot, t)$. We define the discrete Fourier transform (DFT) of $u_N$ as

$$(F u_N)(k) \equiv \widehat{u_N}(k) := \sum_{j_1 = -N/2}^{N/2-1} \sum_{j_2 = -N/2}^{N/2-1} u_N(x_j)\, e^{-2\pi i (k \cdot j)/N}, \quad k \in \mathcal{W}_N. \tag{2.11}$$

Then, the inverse discrete Fourier transform can be defined as

$$(F^{-1}\widehat{u_N})(x_j) \equiv u_N(x_j) := \frac{1}{N^2} \sum_{k_1=-N/2}^{N/2-1} \sum_{k_2=-N/2}^{N/2-1} \widehat{u_N}(k) e^{2\pi i (k\cdot j)/N} \quad x_j \in \mathcal{T}_N. \tag{2.12}$$

Consequently, a discrete version of the $\mathrm{H}^s(\mathbb{T}^2)$-norm in (2.4) can now be defined.

**Definition 2.11** (Discrete Sobolev Norm)**.** *Let $N \geq 2$ be an even integer and let $u_N$ be a discrete function defined on $\mathcal{T}_N$ (cf.* (2.9)*). The discrete $\mathrm{H}^s(\mathbb{T}^2)$-norm of $u_N$ is defined as*

$$|\!|\!| u_N |\!|\!|_s^2 := \frac{h^2}{N^2} \sum_{k_1=-N/2}^{N/2-1} \sum_{k_2=-N/2}^{N/2-1} \langle\, k \,\rangle^{2s} \, |\widehat{u_N}(k)|^2, \tag{2.13}$$

*where $h := 2\pi/N$ is the grid spacing.*

**Remark 2.12.** *The factor $h^2/N^2$ in* (2.13) *corresponds to a necessary scaling so that this norm becomes a proper approximation to the $\mathrm{H}^s(\mathbb{T}^2)$ norm. Consider, for instance, the case $s = 0$. Since the DFT defined in* (2.11) *induces the following Parseval's identity:*

$$\sum_{j_1=-N/2}^{N/2-1} \sum_{j_2=-N/2}^{N/2-1} |u_N(x_j)|^2 = \frac{1}{N^2} \sum_{k_1=-N/2}^{N/2-1} \sum_{k_2=-N/2}^{N/2-1} |\widehat{u_N}(k)|^2, \tag{2.14}$$

*there holds*

$$\begin{aligned} |\!|\!| u_N |\!|\!|_0^2 &= \frac{h^2}{N^2} \sum_{k_1=-N/2}^{N/2-1} \sum_{k_2=-N/2}^{N/2-1} |\widehat{u_N}(k)|^2 \\ &= \left(\frac{2\pi}{N}\right)^2 \sum_{j_1=-N/2}^{N/2-1} \sum_{j_2=-N/2}^{N/2-1} |u_N(x_j)|^2 \xrightarrow{N\to\infty} \int_{\mathbb{T}^2} |u|^2 \, dx = \| u \|_0^2. \end{aligned}$$

Next, in order to illustrate how some of the statements in Theorem 2.9 manifest in the numerical experiments (and in particular, the regularity of an approximation $u_N(x,t)$), we have a look at how their corresponding Fourier coefficients decay. For this two-dimensional case, the analysis can be done in a radial fashion (see, e.g., [6, 38]).

**Definition 2.13** (Radial energy density (RED))**.** *Let $N \geq 4$ be an even integer and $u_N$ be a discrete function defined on the $N^2$ grid points of $\mathbb{T}^2$. The radial energy density (RED) $E_s$ is defined as*

$$E_s[u_N](R) := \frac{1}{N^2} \sum_{k \in A_R \cap \mathbb{Z}^2} \langle\, k \,\rangle^{2s} \, |\widehat{u_N}(k)|^2, \quad R = 2, 4, 6, \ldots, \frac{N}{2}. \tag{2.15}$$

*where $A_R := \Big\{ x \in \mathbb{R}^2 : R - 2 \leq |x| < R \Big\}$ is the $R$-th annulus of width 2 in $\mathbb{R}^2$ (see Figure 2.1).*

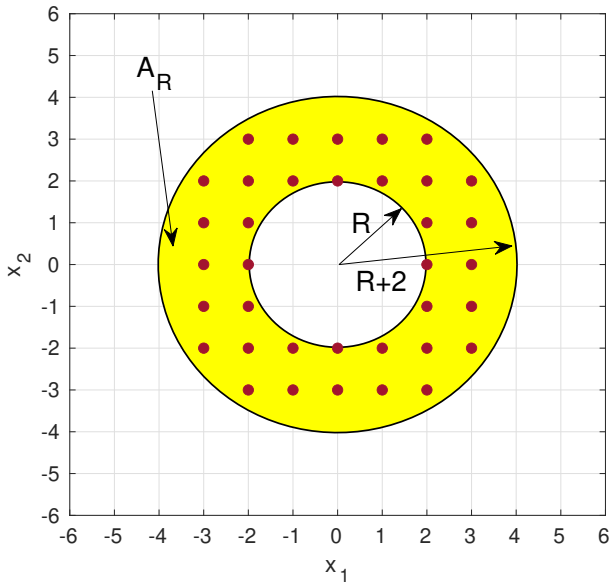


Figure 2.1: Annulus $A_R$ in Definition 2.13 (in yellow), with the set $A_R \cap \mathbb{Z}^2$ shown in red dots.

**Remark 2.14.** *From the previous definition, we readily see that*

$$h^2 \sum_{l=1}^{N/4} E_s[u_N](2l) \leq \frac{h^2}{N^2} \sum_{k_1=-N/2}^{N/2-1} \sum_{k_2=-N/2}^{N/2-1} \langle\, k \,\rangle^{2s} \, |\widehat{u_N}(k)|^2 = |||\, u_N \,|||_s^2,$$

*and therefore, for large $N$ and $s \in \mathbb{R}$, if $u_N \in \mathrm{H}^s(\mathbb{T}^2)$ then the series $\sum_{l=1}^{\infty} E_s[u_N](2l)$ must converge.*

## 2.4 A pseudo-spectral method

In order to make sense of the differential part of (2.5), we use the definition of $P$ (cf. (2.6)) and the Fourier transform (2.1) to rewrite the evolution problem in Fourier space as

$$i\widehat{u}_t - \langle\, \xi \,\rangle^{-1} \xi_2 \widehat{u} + r\, \widehat{\beta} * \widehat{u} = \widehat{f} e^{-i\omega_0 t} \quad \text{in } \mathbb{Z}^2 \times (0,\infty), \quad \widehat{u}\big|_{t=0} = 0. \tag{2.16}$$

To avoid the computation of the convolution in (2.16), we use a pseudo-spectral approach to discretize the problem, that is, we approximate $u(x,t) \approx u_N(x,t)$, with

$$u_N(x_j,t) = \frac{1}{N^2} \sum_{k_1=-N/2}^{N/2-1} \sum_{k_2=-N/2}^{N/2-1} \widehat{u_N}(k,t) e^{-2\pi i (k\cdot x_j)/N},$$

where $j = (j_1, j_2)$, $j_\iota = -N/2, \ldots, N/2-1$, $\iota = 1,2$, $t > 0$ and $\widehat{u_N}(k,t)$ are Fourier coefficients computed using the DFT defined in (2.11). Therefore, a semi-discretization (in

the form of the method of lines) for (2.16) yields

$$i\,\partial_t \widehat{u_N} - \langle\, k\,\rangle^{-1} k_2\, \widehat{u_N} + rF\left(\beta\, F^{-1}\widehat{u_N}\right) = \widehat{f} e^{-i\omega_0 t} \qquad k \in \mathcal{W}_N,\ t > 0. \tag{2.17}$$

Here, $\widehat{u_N}(k,0) = 0$ and $\widehat{f}$ is now the DFT of $f$ (evaluated at the grid points). We then have a system of $N^2$ decoupled ODEs,

$$\frac{\mathrm{d}}{\mathrm{d}t}\widehat{U_N}(t) = \mathbf{L} \odot \widehat{U_N}(t) + \mathbf{N}(\widehat{U_N}, t) \qquad t \in (0, T] \tag{2.18}$$

where $\odot$ is the classic Hadamard (component-wise) product of matrices, $T > 0$ is a final time, and for each $t \in [0,T]$, $\widehat{U_N}(t) \in \mathbb{C}^{N\times N}$ is a matrix array of the Fourier coefficients $\widehat{u_N}(m,n,t)$, with $(m,n) \in \mathcal{W}_N$; the components of the matrix $\mathbf{L}$ are

$$L_{m,n} := -\frac{in}{\sqrt{1+m^2+n^2}}, \quad (m,n) \in \mathcal{W}_N, \tag{2.19}$$

and $\mathbf{N}$ is a matrix given by

$$\mathbf{N}(\widehat{U_N}, t) := irF\Big(\beta\, F^{-1}\widehat{u_N}\Big) - i\widehat{f} e^{-i\omega_0 t}. \tag{2.20}$$

In this way, we find an approximation to the solution of (2.5) by taking the inverse DFT of the solution to (2.18) at each time.

## 2.5 Time-stepping schemes

Notice first that, given the nonlinearity present in (2.18) (coming from the term $F(\beta F^{-1}\widehat{u_N})$ in (2.17)), it would be convenient to use an explicit time-stepping scheme to fully discretize this system. In addition, we would like to pair our pseudo-spectral method with a high-order time discretization. It is known, however, that a certain time-step restriction would appear in this case.

To analyze what kind of time-steps $\Delta t$ we should expect to take, let us view the system (2.18) as a traditional system of ODEs where $\widehat{U_N}$ is a vector of unknowns and $\mathbf{L}$ is a diagonal matrix in $\mathbb{C}^{N^2\times N^2}$ with diagonal entries given by (2.19). In this scenario, the eigenvalues of $\mathbf{L}$ are precisely such entries. Moreover, since

$$|L_{m,n}| \le 1 \quad \forall\, (m,n) \in \mathcal{W}_N,$$

the classical fourth-order Runge-Kutta scheme, for instance, would yield a time-step restriction

$$\Delta t < 2.8, \tag{2.21}$$

(see, e.g., [43]).

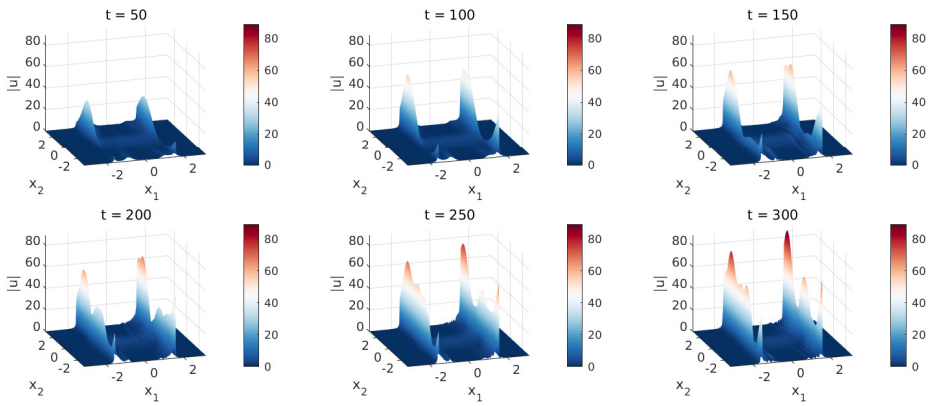


Figure 2.2: Computed approximation to the solution of (2.5) using the RK4 time-stepping ($\Delta t = 0.5$) and a mesh with $N = 256$ points in each direction.

As a second alternative, we may have a look at A-stable schemes, for which no time restrictions appear from the linear part. Indeed, we begin by ruling out multistep methods, as their accuracy is at most second order (as per Dalhquist's second barrier theorem, cf. [11]). Then, as the problem is of dispersive-type (the eigenvalues of the linear part are purely imaginary), we may explore schemes that have been used in other dispersive equations, such as the Korteweg-de-Vries (KdV), the Kadomtsev-Petviashvili, and the nonlinear Schrödinger (NLS) equations. In particular, the Exponential Time-Differencing method with RK4 time-stepping (ETDRK4, cf. [10]) has proven to be a good A-stable method to approximate the solution to the KdV and NLS-type equations (cf., e.g., [24, 27]). A first result is portrayed in Figure 2.2, where we have considered $\omega_0 = 0$, $r = 2$, $\beta(x) = \cos(x_1)$ and $f(x) = -5\exp\big(-|x|^2 + i(2x_1 + x_2)\big)$. Here, we immediately notice the presence of two attractors: one at $x_1 = -\pi/2$ and another one at $x_1 = \pi/2$, in agreement with the description of the attracting Lagrangians in [17] for this scenario (the reason why we expect attractors at these locations will become clearer after introducing some dynamical aspects in Section 4.1). From now on, the transient solutions will be computed using the ETDRK4 scheme, unless otherwise specified.

## 2.6 Convergence studies

We now proceed to test the convergence of the methods so far presented. First, we consider $\omega_0 = 0.1$, $T = 10$, $r = 2$, $\beta = \cos(x_1)$ and $f = f_4$, where

$$f_4(x) = -5\exp\Big(-3\big((x_1 + 0.9)^2 + (x_2 + 0.8)^2\big) + i\big(2x_1 + x_2\big)\Big). \tag{2.22}$$

We fix a spatial mesh with $N = 64$ grid points per direction, and take several choices of time steps $\Delta t = 1, \frac{1}{2^1}, \frac{1}{2^2}, \ldots, \frac{1}{2^8}$. To test the robustness of our code, the peak of the Gaussian

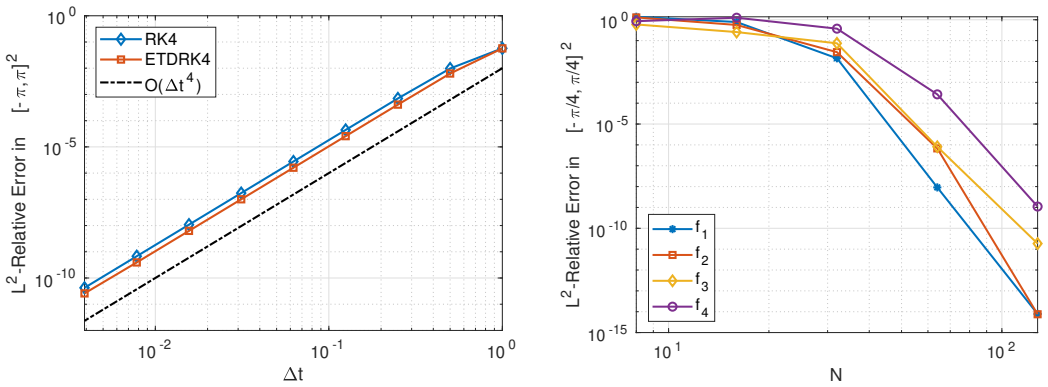


Figure 2.3: Convergence studies. Left: fourth-order convergence in time. Right: local spectral accuracy in space.

in (2.22) has been purposely set closer to the attractor $x_1 = -\pi/2$. We observe in Figure 2.3 (left) the expected fourth-order convergence, with the ETDRK4 method performing slightly better than the traditional RK4. Here, the error has been measured at the final time using the $|||\cdot|||_0$ norm (over the whole domain) defined in (2.13), and with respect to a more refined solution (same $N$ but with $\Delta t = 2^{-10} \cdot 10^{-2} \approx 10^{-5}$).

While the decay in the error curves shown in Figure 2.3 (left) is enough to show convergence in time, the study in space has to be done more carefully. Indeed, as $u \notin C(0,\infty;\mathrm{L}^2(\mathbb{T}^2))$, and for fixed time $t > 0$, there is no guarantee that $u(\cdot,t)$ is smoother than $\mathrm{L}^2(\mathbb{T}^2)$, global spectral accuracy cannot be expected. However, Figure 2.2 shows that in regions that are away from the attractors (located near $x_1 = \pm\pi/2$), the solution does appear to be smooth. Hence, we measure the $\mathrm{L}^2$-error with respect to a more refined solution ($N = 2^{10}$) in the domain $[-\pi/4, \pi/4]^2$. For this experiment we have fixed the time step at $\Delta t = 0.01$ and considered the ETDRK4 time-stepping method. Similarly to the study in time, we have taken $\omega_0 = 0.5$, $T = 10$, $r = 2$, $\beta(x) = \cos(x_1)$. We take values of $N = 2^3, 2^4, \ldots, 2^7$ per spatial direction and also consider several source terms (with different levels of easiness of resolution):

$$f_1(x) = \sin(x_1)\cos(2x_2), \tag{2.23}$$

$$f_2(x) = \sin(x_1)\cos(2x_2) + \sin(5x_1)\cos(2x_2) + i\sin(5x_1)\cos(4x_2), \tag{2.24}$$

$$f_3(x) = \frac{1}{2}\exp\big(-2|x|^2\big), \tag{2.25}$$

and $f_4$ defined in (2.22). We show these results in Figure 2.3 (right), where we see spectral decay of the error in the region $[-\pi/4, \pi/4]^2$.

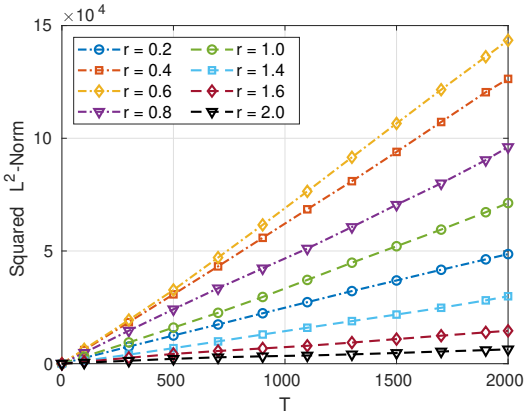


Figure 2.4: Evolution of the squared $\mathrm{L}^2$-norm for several values of $r$ and $\beta(x) = \cos(x_1) + \sin(x_2)$.

## 2.7 Regularity of the approximations

To complement the results shown by the convergence studies, we now focus on verifying that the numerical solutions have the regularity properties that Theorem 2.9 predicts for the continuous problem. First, we show in Figure 2.4 the linearity in the evolution of $|||\, u_N(t)\, |||_0^2$ for different values of $r$ and $\beta(x) = \cos(x_1) + \sin(x_2)$ (the source term is again a centered Gaussian similar to the one used in Figure 2.2). It becomes more evident that $u_\infty \notin \mathrm{L}^2(\mathbb{T}^2)$ when we look at the RED $E_0$ (cf. (2.15)) at different times, as shown in Figure 2.5: while the RED quickly drops to below machine epsilon at the beginning of the simulation, it is not the case as the end time $T$ increases. Finally, we can have a look at how fast the RED decays for several choices of $s$. First, for $s = -1/2$, we observe in Figure 2.6 (left) that the RED decays as $R^{-1}$, which is slow enough to say that $u_\infty \notin \mathrm{H}^{-1/2}(\mathbb{T}^2)$ (per Remark 2.14, since adding all points in the $E_{-1/2}[u_N]$ curve would resemble the harmonic series). However, as soon as we take $s < -1/2$, the RED appears to decay as $R^{2s}$, as shown as in Figure 2.6 (center and right), which suggests that $u_\infty \in \mathrm{H}^s(\mathbb{T}^2)$ for $s < -1/2$.

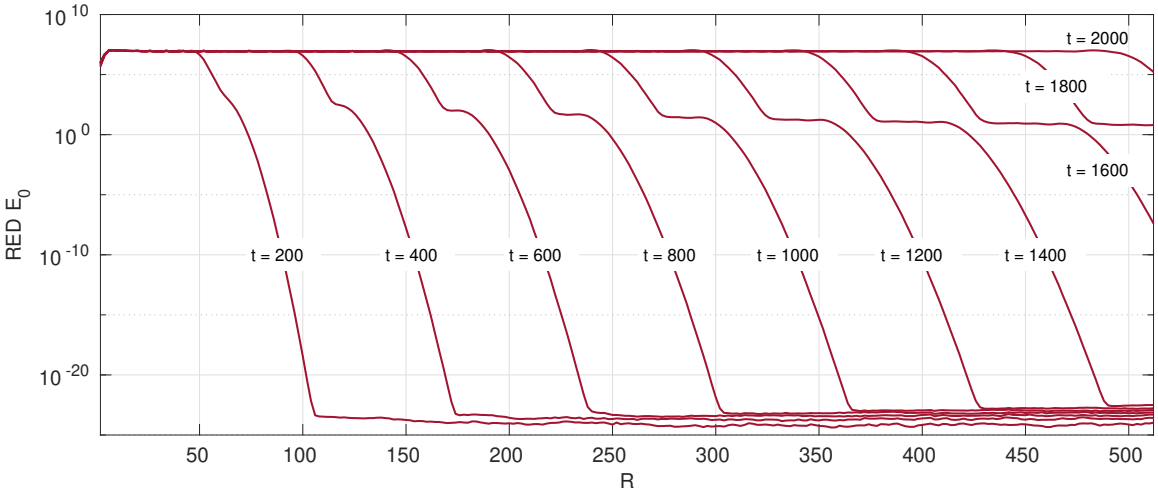


Figure 2.5: Radial energy density $E_0$ at several times ($r = 0.25$, $\beta(x) = \cos(x_1) + \sin(x_2)$).

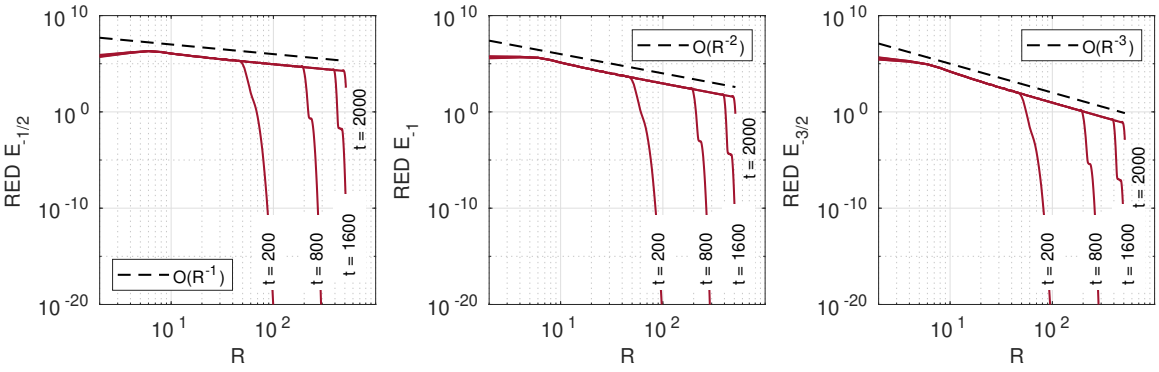


Figure 2.6: Radial energy density for different values of $s$. This suggests that $E_s(u_N)(R)$ decays faster than $R^{2s}$ for any $s \leq 0$.

# Chapter 3

# The Eigenvalue Problem

As pointed out in the introduction to this work, there is belief within the physics community that the attractors present in the transient solution to (2.5) appear as an intrinsic property of the differential operator that defines the evolution (cf., e.g., [35]). This motivates our study of the problem

$$(P(x,D)-\omega_0)u(x)=\lambda u(x), \quad x\in\mathbb{T}^2, \tag{3.1}$$

where $\omega_0\geq 0$ and $P(x,D)$ is the zero-th order operator defined in (2.6), that is,

$$P(x,D)u(x)=\mathcal{F}^{-1}\Big\{\langle\,\xi\,\rangle^{-1}\xi_2\;\widehat{u}(\xi)\Big\}-r\beta(x)u(x). \tag{3.2}$$

We begin this Chapter describing the spectrum $\sigma(P-\omega_0)$. The computation of eigenvalues, however, is challenging since they are embedded in a essential spectrum, as we discuss next. We describe in Section 3.2 a method to distinguish these eigenvalues, and in Section 3.3 we discretize this new problem using tools from Chapter 2. Next, in Section 3.4 we analyze the structure of the resulting matrix. Ultimately in Section 3.5 we develop an accurate strategy to solve this eigenvalue problem.

## 3.1 Essential and pure point spectrum

Notice that, without loss of generality, we can focus on the case $\omega_0=0$, since $\sigma(P-\omega_0)=\sigma(P)-\omega_0$ (by the spectral mapping theorem, cf. [4, Theorem 7.1.9]), so the eigenvalues only get shifted by $\omega_0$. Also, since $P$ is a bounded self-adjoint operator, the spectrum $\sigma(P)$ lies entirely on the real axis (cf., e.g., [4, Corollary 7.2.5]). We can obtain a more precise characterization of the essential spectrum using [8, Lemma 2.1]:

$$\sigma_{\mathtt{ess}}(P)\subset\left[-1-r\max_{\mathbb{T}^2}\beta\,,\,1-r\min_{\mathbb{T}^2}\beta\right]. \tag{3.3}$$

Here, the essential spectrum has to be understood in the sense of Pelinovsky [33], that is, $\sigma_{\mathtt{ess}}(P):=\sigma(P)\backslash\sigma_{\mathtt{d}}(P)$, where the discrete spectrum $\sigma_{\mathtt{d}}(P)$ is the set of all eigenvalues of

$P$ with finite (algebraic) multiplicity and which are isolated points of $\sigma(P)$. In turn, [17] shows that there exists a finite number of eigenvalues, with associated eigenfunctions that are smooth (it was later shown by Wang [44] that these eigenfunctions are, in fact, analytic).

**Lemma 3.1** ([17, Lemma 3.2])**.** *Let $\omega_0 = 0$. There exists $\delta$ sufficiently small such that the cardinality of $\sigma_{\mathtt{pp}}(P) \cap [-\delta, \delta]$ is finite. Furthermore, if $Pu = \lambda u$ for $u \in \mathrm{L}^2(\mathbb{T}^2)$ and $|\lambda| \leq \delta$, then $u \in C^\infty(\mathbb{T}^2)$.*

Here, the pure point spectrum $\sigma_{\mathtt{pp}}(P)$ is the set of all eigenvalues, both embedded and isolated (a precise definition can be made using the spectral measure, cf. [1, §4.3]). This opens the possibility of having eigenvalues that are embedded in the essential spectrum (i.e., at a zero distance from the continuous spectrum $\sigma_{\mathtt{c}}(P)$) given by (3.3), especially when $[-\delta, \delta] \subset \sigma_{\mathtt{ess}}(P)$. In this case, a straightforward discretization of (3.1) would not differentiate between points in $\sigma_{\mathtt{pp}}(P)$ or $\sigma_{\mathtt{ess}}(P)$, so we need to take a different approach such that these elements become distinguishable.

## 3.2 Elliptic perturbation

Let $\Delta$ denote the standard Laplacian operator in $\mathbb{T}^2$. It is known that $-\Delta$ on $\mathbb{T}^2$ has a countable spectrum and numerical techniques for its computation are well known (cf., e.g., [43]). Motivated by this, we consider the small viscosity problem: Find pairs $(\lambda^{(\nu)}, u^{(\nu)})$ such that

$$(P(x, D) + i\nu\Delta)u^{(\nu)}(x) = \lambda^{(\nu)}u^{(\nu)}(x), \quad x \in \mathbb{T}^2, \tag{3.4}$$

where $\nu > 0$ is a "viscosity", and thus, we may refer to (3.4) as the "viscous problem". Notice that $(P + i\nu\Delta)u^{(\nu)}$ can be written as

$$(P(x, D) + i\nu\Delta)u^{(\nu)}(x) = \mathcal{F}^{-1}\Big\{\widetilde{p}(\xi; \nu)\ \widehat{u^{(\nu)}}(\xi)\Big\} - r\beta(x)u^{(\nu)}(x),$$

where, for fixed $\nu$, $\widetilde{p}(\,\cdot\,; \nu)$ is the symbol of order 2:

$$\widetilde{p}(\xi; \nu) := \langle\, \xi \,\rangle^{-1}\xi_2 - i\nu|\xi|^2, \quad \xi = (\xi_1, \xi_2) \in \mathbb{Z}^2. \tag{3.5}$$

Since $P + i\nu\Delta$ is a second-order pseudo-differential operator that is not self-adjoint, it is likely that the eigenvalues will not lay on the real axis. In this way, using the main result from [18], we can obtain some hints on how we can use the viscous problem to find the embedded eigenvalues of $P$.

**Theorem 3.2.** *Let $P$ be the operator defined by* (3.2)*. Then, there exists an open neighbourhood $U$ of $0$ in $\mathbb{C}$, and a set*

$$\mathscr{R}(P) \subset \{z \in \mathbb{C} : \mathrm{Im}(z)\ \leq 0\} \cap U,$$

*such that for every set $K$ compactly contained in $U$, $\mathscr{R}(P) \cap K$ is discrete and*

$$\sigma_{\mathtt{pp}}(P + i\nu\Delta) \longrightarrow \mathscr{R}(P) \quad \textit{as } \nu \to 0^+,$$

*uniformly on $K$. Furthermore,*

$$\mathscr{R}(P) \cap \mathbb{R} = \sigma_{\mathtt{pp}}(P) \cap U.$$

The convergence in Theorem 3.2 has to be understood as the convergence of a sequence of functions $\{f_\nu\}_{\nu>0}$ as $\nu \to 0^+$ whose zeros are precisely the eigenvalues of the viscous operator. More precisely, according to [18, Lemma 7.7], there exists an open set $\Omega \subset \mathbb{C}$ and a sequence of functions $f_\nu : \Omega \to \mathbb{C}$ such that the eigenvalues of $P + i\nu\Delta$ agree (with multiplicity) with the zeros of $f_\nu$. The result can then be proved by showing that for all $\omega \in \Omega$,

$$|f_\nu(\omega) - f_0(\omega)| \to 0 \quad \text{as } \nu \to 0^+.$$

In addition, we can write $\mathscr{R}(P) = \{\lambda_j\}_{j=1}^N$, where $N = \infty$ is allowed. This is because $\mathscr{R}(P)$ not only contains some of the embedded eigenvalues of $P$ but also elements from the resolvent set $\rho(P) := \mathbb{C}\backslash\sigma(P)$. Hence, this theorem suggests that for $\sigma_{\mathtt{pp}}(P + i\nu\Delta) = \left\{\lambda_j^{(\nu)}\right\}_{j=1}^\infty$, we have (after suitable reordering)

$$\lambda_j^{(\nu)} \longrightarrow \lambda_j \quad \text{as } \nu \to 0^+, \tag{3.6}$$

uniformly on compact sets and with agreement of multiplicities. This means that, by tracking the limit $\nu \to 0^+$, we should be able to find some of the embedded eigenvalues of $P$.

Another important fact to notice is that while the eigenfunctions associated to the embedded eigenvalues of $P$ are analytic, those related to $P + i\nu\Delta$ (for fixed $\nu$) might not even be functions. Indeed, [18, Theorem 2] affirms that there exists $\widetilde{\delta} > 0$ such that these eigenmodes are in a Hilbert space $\mathcal{X}$ that satisfies:

$$\mathscr{A}_{\widetilde{\delta}} \subset \mathcal{X} \subset \mathscr{A}_{-\widetilde{\delta}}, \tag{3.7}$$

where for any $s \geq 0$, $\mathscr{A}_{-s}$ is the dual of the space $\mathscr{A}_s$, defined as

$$\mathscr{A}_s := \left\{ u \in \mathrm{L}^2(\mathbb{T}^2) : \sum_{\xi \in \mathbb{Z}^2} |\widehat{u}(\xi)|^2 e^{4|\xi|s} < \infty \right\}.$$

## 3.3 Discretization

We now focus on constructing a discretization of the viscous problem (3.4), using the pseudo-spectral techniques considered in Chapter 2.

Let $\mathbf{F}_1$ denote the matrix that defines the one-dimensional DFT of size $N$ (defined in an analogous way to (2.11)), and let $v$ be a grid function defined on the mesh $\mathcal{T}_N$ (cf. Definition 2.10) as

$$v = \begin{bmatrix} v\left(x_{-\frac{N}{2},-\frac{N}{2}}\right) & v\left(x_{-\frac{N}{2}+1,-\frac{N}{2}}\right) & \cdots & v\left(x_{\frac{N}{2}-1,-\frac{N}{2}}\right) \\ v\left(x_{-\frac{N}{2},-\frac{N}{2}+1}\right) & v\left(x_{-\frac{N}{2}+1,-\frac{N}{2}+1}\right) & \cdots & v\left(x_{\frac{N}{2}-1,-\frac{N}{2}+1}\right) \\ \vdots & \vdots & \ddots & \vdots \\ v\left(x_{-\frac{N}{2},\frac{N}{2}-1}\right) & v\left(x_{-\frac{N}{2}+1,\frac{N}{2}-1}\right) & \cdots & v\left(x_{\frac{N}{2}-1,\frac{N}{2}-1}\right) \end{bmatrix}. \tag{3.8}$$

In addition, denote by $\mathbf{v} \in \mathbb{C}^{N^2\times 1}$ the column-wise rearranged version of the matrix $v$. Then, the two-dimensional DFT (2.11) can be computed as

$$\widehat{\mathbf{v}} = \mathbf{F}_2\mathbf{v}, \quad \mathbf{F}_2 := \mathbf{F}_1 \otimes \mathbf{F}_1 \in \mathbb{C}^{N^2\times N^2},$$

where $\otimes$ denotes the Kronecker product of matrices. In turn, the inverse DFT can then be computed as

$$\mathbf{v} = \mathbf{F}_2^{-1}\widehat{\mathbf{v}} = \frac{1}{N^2}\mathbf{F}_2^*\widehat{\mathbf{v}}.$$

Therefore, following the same techniques as in Section 2.4, the problem (3.4) can be discretized as

$$\left(\mathbf{D}_\nu - r\mathbf{F}_2\mathbf{B}\mathbf{F}_2^{-1}\right)\widehat{\mathbf{u}}_N^{(\nu)} = \lambda^{(\nu)}\widehat{\mathbf{u}}_N^{(\nu)}. \tag{3.9}$$

Here, $\mathbf{D}_\nu$ consists of the evaluations $\widetilde{p}(k;\nu)$ (cf. (3.5)) for $k \in \mathcal{W}_N$ (cf. Definition 2.10). It is a block diagonal matrix described as:

$$\mathbf{D}_\nu = \left[\begin{array}{c|c|c|c|c} \mathbf{D}_{\nu,1} & & & & \\ \hline & \ddots & & & \\ \hline & & \mathbf{D}_{\nu,l} & & \\ \hline & & & \ddots & \\ \hline & & & & \mathbf{D}_{\nu,N} \end{array}\right], \quad \mathbf{D}_{\nu,l} = \begin{bmatrix} d_{\nu,l}^{(1)} & & & \\ & d_{\nu,l}^{(2)} & & \\ & & \ddots & \\ & & & d_{\nu,l}^{(N)} \end{bmatrix},$$

where

$$d_{\nu,l}^{(j)} = \widetilde{p}\left(-\frac{N}{2}+l-1\,,\,-\frac{N}{2}+j-1\,;\,\nu\right), \quad l,j = 1,\ldots,N.$$

Similarly, the entries $\mathbf{B}$ corresponds to evaluations of $\beta$ at the grid points $x_j \in \mathcal{T}_N$ (cf. Definition 2.10). It is also a block diagonal matrix given by:

$$\mathbf{B} = \begin{bmatrix} \mathbf{B}_1 & & & & \\ & \ddots & & & \\ & & \mathbf{B}_l & & \\ & & & \ddots & \\ & & & & \mathbf{B}_N \end{bmatrix}, \quad \mathbf{B}_l = \begin{bmatrix} b_l^{(1)} & & & \\ & b_l^{(2)} & & \\ & & \ddots & \\ & & & b_l^{(N)} \end{bmatrix},$$

where

$$b_l^{(j)} = \beta\left(x_{-N/2+l-1,-N/2+j-1}\right), \quad l, j = 1, \ldots, N. \tag{3.10}$$

## 3.4 Matrix structure and computational challenges

Since $\mathbf{D}_\nu$ is a diagonal (albeit non-hermitian) matrix, we will focus instead on the structure of $\mathbf{F}_2\mathbf{B}\mathbf{F}_2^*$. First, it can be shown that $\mathbf{F}_2\mathbf{B}\mathbf{F}_2^*$ is a block-circulant matrix. Indeed, we first have that

$$\mathbf{F}_1 = \left[w_N^{(r-1)(s-1)}\right]_{r,s=1}^N \quad \text{with } w_N := \exp(-2\pi i/N).$$

Then, the $(p, q)$ block of $\mathbf{F}_2\mathbf{B}\mathbf{F}_2^*$ is given by

$$(\mathbf{F}_2\mathbf{B}\mathbf{F}_2^*)_{p,q} = \sum_{l=1}^N w_N^{(p-1)(l-1)}\, \overline{w_N}^{(l-1)(q-1)} \mathbf{F}_1\mathbf{B}_l\mathbf{F}_1^*, \tag{3.11}$$

where $\mathbf{B}_l$ is the $l$-th $N$-by-$N$ diagonal block of $\mathbf{B}$. Moreover,

$$(\mathbf{F}_1\mathbf{B}_l\mathbf{F}_1^*)_{r,s} = \sum_{j=1}^N w_N^{(r-1)(j-1)}\, \overline{w_N}^{(j-1)(s-1)}\, b_l^{(j)} \tag{3.12}$$

with $b_l^{(j)}$ being the $j$-th diagonal component of $\mathbf{B}_l$ defined in (3.10). Using that $\overline{w}_N^d = w_N^{-d}$ for any $d \in \mathbb{R}$, it is possible to prove that $\mathbf{F}_1\mathbf{B}_l\mathbf{F}_1^*$ is banded:

$$(\mathbf{F}_1\mathbf{B}_l\mathbf{F}_1^*)_{r,r+p} = \sum_{j=1}^N b_l^{(j)}\, \overline{w_N}^p,$$

for any $p$ (the expression on the right-hand side is independent of $r$), and by looking at the first row and column,

$$(\mathbf{F}_1\mathbf{B}_l\mathbf{F}_1^*)_{N-p,1} = (\mathbf{F}_1\mathbf{B}_l\mathbf{F}_1^*)_{1,2+p}, \quad \forall\, p = 0, 1, \ldots, N-2,$$

we obtain that the matrix $\mathbf{F}_1\mathbf{B}_l\mathbf{F}_1^*$ is circulant. Therefore, using a similar argument in (3.11), we deduce that $\mathbf{F}_2\mathbf{B}\mathbf{F}_2^*$ is block-circulant.

### 3.4.1 Sparsity and round-off errors

If $\beta$ has a small amount of Fourier modes, and the computations are done in exact arithmetic, $\mathbf{F}_2\mathbf{B}\mathbf{F}_2^*$ should be a sparse matrix. Indeed, the first column of $\mathbf{F}_1\mathbf{B}_l\mathbf{F}_1^* =: \widehat{\mathbf{B}_l}$ corresponds to a one-dimensional DFT applied to the diagonal elements of $\mathbf{B}_l$ (i.e., $\beta(x_{l,1}), \ldots, \beta(x_{l,N})$). Thus, under such assumption for $\beta$, the output of these DFTs should be vectors with only a handful of nonzero components, and hence the matrices $\widehat{\mathbf{B}_l}$ should be relatively sparsely banded. We could then expect the first block-column of $\mathbf{F}_2\mathbf{B}\mathbf{F}_2^*$ (cf (3.11)) to be sparse as well, since this can be computed as

$$(\mathbf{F}_1 \otimes \mathbf{I}) \begin{pmatrix} \widehat{\mathbf{B}_1} \\ \vdots \\ \widehat{\mathbf{B}_N} \end{pmatrix}, \tag{3.13}$$

with $\mathbf{I}$ being the $N$-by-$N$ identity matrix. However, because of round-off errors coming from the sampling of $\beta$ and the computation of first set of DFTs, the blocks $\widehat{\mathbf{B}_l}$ will be dense matrices, and so will be the product by $\mathbf{F}_1 \otimes \mathbf{I}$, making the computation of the eigenvalues of $\mathbf{D}_\nu - r\mathbf{F}_2\mathbf{B}\mathbf{F}_2^{-1}$ costly in computational terms. Therefore, it is a matter for future work to derive an efficient strategy that can take advantage of any possible sparsity in the Fourier transform of $\beta$.

**Example 3.3.** Consider the grid functions

$$\mathrm{B}_n = \begin{bmatrix} -1 & -6.12 \cdot 10^{-17} & 1 & -6.12 \cdot 10^{-17} \\ -2 & -1 & 0 & -1 \\ -1 & 6.12 \cdot 10^{-17} & 1 & 6.12 \cdot 10^{-17} \\ 0 & 1 & 2 & 1 \end{bmatrix}, \quad \mathrm{B}_e = \begin{bmatrix} -1 & 0 & 1 & 0 \\ -2 & -1 & 0 & -1 \\ -1 & 0 & 1 & 0 \\ 0 & 1 & 2 & 1 \end{bmatrix},$$

which correspond to the function $\beta(x) = \cos(x_1) + \sin(x_2)$ sampled at $x_1, x_2 = -\pi, -\frac{\pi}{2}, 0, \frac{\pi}{2}$ in floating-point and exact arithmetic, respectively. Then, computing the DFT of the columns using the Fast Fourier Transform (FFT) for $\mathrm{B}_n$ and a direct and exact computation for $\mathrm{B}_e$ yields

$$\widehat{\mathrm{B}_n} = \begin{bmatrix} -4 & 1.11 \cdot 10^{-16} & 4 & 1.11 \cdot 10^{-16} \\ -2.22 \cdot 10^{-16} + 2i & -1.22 \cdot 10^{-16} + 2i & -1.11 \cdot 10^{-16} + 2i & -1.22 \cdot 10^{-16} + 2i \\ 0 & -1.11 \cdot 10^{-16} & 0 & -1.11 \cdot 10^{-16} \\ -2.22 \cdot 10^{-16} - 2i & -1.22 \cdot 10^{-16} - 2i & -1.11 \cdot 10^{-16} - 2i & -1.22 \cdot 10^{-16} - 2i \end{bmatrix},$$

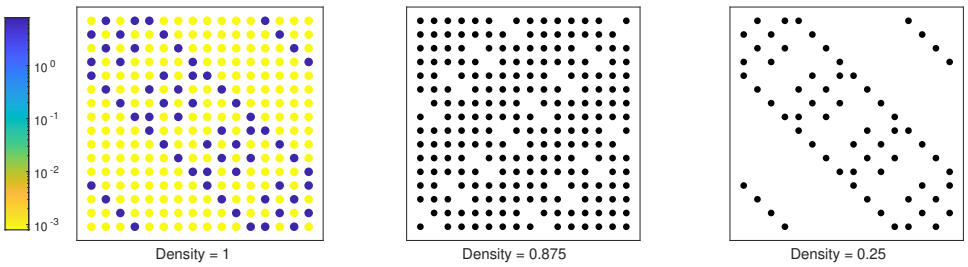


Figure 3.1: Visualization of the density of $\mathbf{F}_2\mathbf{B}\mathbf{F}_2^* \in \mathbb{C}^{16\times 16}$ when computed using the two-dimensional DFT (left), one-dimensional FFTs (center) and one-dimensional DFTs but computed in exact arithmetic (right). The figure in the left is a colored plot of the magnitude of matrix entries, while the center and right figures only indicates the nonzero entries.

| | $N = 4$ | $N = 8$ | $N = 16$ | $N = 32$ | $N = 64$ |
|---|---|---|---|---|---|
| FFT | 87.50% | 96.88 % | 96.88 % | 99.61 % | 99.90 % |
| Exact DFT | 25.00 % | 17.19 % | 12.89 % | 7.52 % | 4.18 % |

Table 3.1: Density (in percentage) of the matrix $\mathbf{F}_2\mathbf{B}\mathbf{F}_2^*$ when the DFT is computed using the Fast Fourier Transform (FFT) versus when it is computed using exact arithmetic.

and

$$\widehat{\mathrm{B}_e} = \begin{bmatrix} -4 & 0 & -4 & 0 \\ 2i & 2i & 2i & 2i \\ 0 & 0 & 0 & 0 \\ -2i & -2i & -2i & -2i \end{bmatrix}.$$

As expected, roundoff errors propagate throughout the computations. Since the columns in these matrices are the main ingredient to construct the circulant blocks $\widehat{\mathbf{B}_l}$, these matrices will also be full. Moreover, performing the multiplication in (3.13) produces matrices $\mathbf{F}_2\mathbf{B}\mathbf{F}_2^*$ that are mostly full as well. Indeed, Figure 3.1 portrays the density (defined as the number of nonzero entries divided by the total number of entries) of these matrices. In addition, as we increase the number of grid points per direction $N$, the situation becomes worse. For $N = 64$, the matrix $\mathbf{F}_2\mathbf{B}\mathbf{F}_2^*$ computed using the FFT yields a density (in percentage) of 99.9%, compared a density of 4.18% when the sampling of $\beta$ and the column-wise DFTs are computed using exact arithmetic (see Table 3.1).

## 3.5 Solution strategy and convergence study

To solve (3.9), we use Matlab's built-in tool `eigs`, which uses an Arnoldi-type iteration to find a subset of eigenvalues of interest. Here, we choose to compute those that are close to 0 (in view of Theorem 3.2) and these are returned in "magnitude-then-phase" ordering, that is, first the eigenvalues are ordered in increasing magnitude, and if two eigenvalues have

the same magnitude, the one with smallest phase (in the interval $(-\pi, \pi]$) appears first. However, in many cases, further ways of sorting will be needed in order to properly track $\lambda_j^{(\nu)}$ as a curve depending on the parameter $\nu$.

**Example 3.4.** Consider $r = 0.5$, $\beta(x) = \cos(x_1) + \sin(x_2)$, $N = 40$ and $\nu = 0.015$. Then, the eigensolver computes the first 8 eigenvalues of (3.9) as (we drop the superscript $(\nu)$ for readability purposes):

$$\big(\lambda_j\big)_{j=1}^{8} = \begin{pmatrix} 0.0166 - 0.1905\text{i} \\ -0.0166 - 0.1905\text{i} \\ -0.0369 - 0.2734\text{i} \\ 0.0369 - 0.2734\text{i} \\ -0.0401 - 0.3252i \\ 0.0401 - 0.3252i \\ 0.2518 - 0.2424\text{i} \\ -0.2518 - 0.2424\text{i} \end{pmatrix}, \qquad \big(|\lambda_j|\big)_{j=1}^{8} = \begin{pmatrix} 0.191246980677908 \\ 0.191246980677910 \\ 0.275887857562819 \\ 0.275887857562819 \\ 0.327685703948980 \\ 0.327685703948985 \\ 0.349551258136058 \\ 0.349551258136059 \end{pmatrix}.$$

It appears then that, in this case, both $\lambda$ and $-\overline{\lambda}$ are eigenvalues of $P + i\nu\Delta$. If $\operatorname{Re}\lambda > 0$, then according to the sorting method described previously, $-\overline{\lambda}$ should always appear first. This is true for the pair $(\lambda_3, \lambda_4)$, however, the pairs $(\lambda_1, \lambda_2)$ and $(\lambda_7, \lambda_8)$ fail to follow this order. By looking at the magnitude of these eigenvalues, we find that this discrepancy comes from very small differences (of the order $10^{-15}$) in these magnitudes.

This phenomenon is prone to cause difficulties when trying to examine the limit $\nu \to 0^+$ (cf. (3.6)). Therefore, we consider (and set by default) an additional sorting step by reordering these eigenvalues so that those with nonnegative real part appear first. In the previous example, the final result would look like:

$$\begin{pmatrix} 0.0166 - 0.1905i \\ -0.0166 - 0.1905i \\ -0.0369 - 0.2734i \\ 0.0369 - 0.2734i \\ -0.0401 - 0.3252i \\ 0.0401 - 0.3252i \\ 0.2518 - 0.2424i \\ -0.2518 - 0.2424i \end{pmatrix} \longrightarrow \begin{pmatrix} 0.0166 - 0.1905i \\ 0.0369 - 0.2734i \\ 0.0401 - 0.3252i \\ 0.2518 - 0.2424i \\ -0.0166 - 0.1905i \\ -0.0369 - 0.2734i \\ -0.0401 - 0.3252i \\ -0.2518 - 0.2424i \end{pmatrix}.$$

Note that this way of sorting the eigenvalues would not work if, for instance, there is an eigenvalue with zero real part (as this 0 could manifest as, say, $+10^{-16}$ or $-10^{-16}$). If this happens, then a different reordering must be considered.

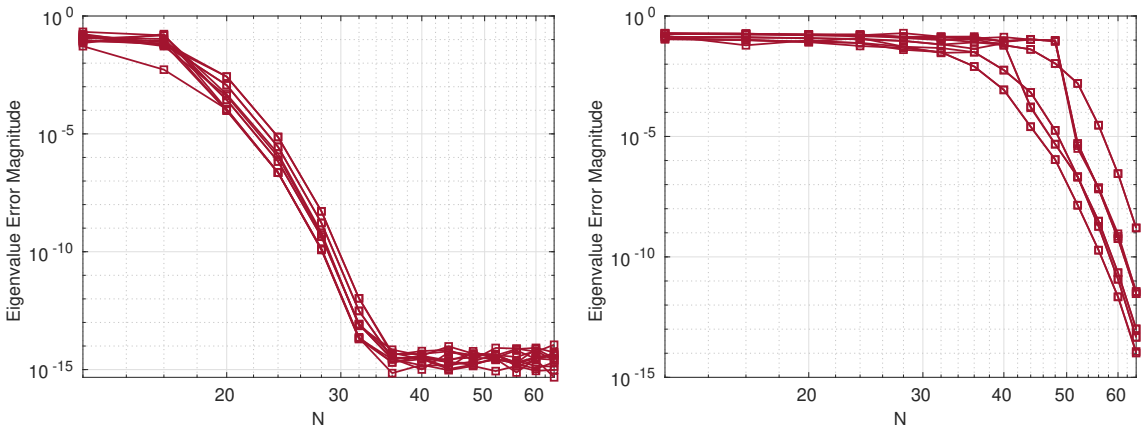


Figure 3.2: Spectral convergence of the first 12 eigenvalues for $\nu = 0.01$ (left) and $\nu = 0.001$ (right).

We finish this section by verifying that our algorithm is convergent. Indeed, we track the error in the first 12 eigenvalues $\left\{\lambda_{N,j}^{(\nu)}\right\}_{j=1}^{12}$ for different values of $N = 12, 16, 20, \ldots, 64$ with respect to a more refined set obtained with $N = 80$. Here, we fix $r = 0.5$, $\beta(x) = \cos(x_1) + \sin(x_2)$ and take $\nu = 0.01$ and $\nu = 0.001$. We can then see in Figure 3.2 that the error $\left|\lambda_{N,j}^{(\nu)} - \lambda_{80,j}^{(\nu)}\right|$ decays spectrally fast in $N$, in agreement with the possible smoothness of the eigenfunctions that is expected thanks to the elliptic perturbation (cf. (3.7)).

# Chapter 4

# Viscosity Limits, Long-term Evolution and Attractors

In this chapter, we provide numerical evidence of a relationship between the internal wave attractors described in Chapter 2 and the spectra of zero-th order pseudo-differential operators discussed in Chapter 3. More precisely, we will explore how the eigenfunctions of the self-adjoint, zeroth-order pseudo-differential operator

$$P(x,D) = \langle D \rangle^{-1} D_{x_2} - r\beta(x), \quad x = (x_1, x_2) \in \mathbb{T}^2, \tag{4.1}$$

(as in (2.6)) partially characterize the solution to the evolution problem

$$iu_t - Pu = fe^{-i\omega_0 t} \quad \text{in } \mathbb{T}^2 \times (0,\infty), \quad u\big|_{t=0} = 0, \tag{4.2}$$

and how they may impact the long-term behaviour of the solution.

We recall that if $P$ is a self-adjoint elliptic operator, the spectrum $\sigma(P)$ completely characterizes the solution to (4.2) (cf. [30]). Indeed, as a motivation to our study, let us consider the linear Schrödinger equation with monochromatic forcing:

$$iu_t + \Delta u = fe^{-i\omega_0 t} \quad \text{in } \mathbb{T}^2 \times (0,\infty), \quad u\big|_{t=0} = 0. \tag{4.3}$$

It is known that the Laplacian operator $-\Delta$ has a countable spectrum $\{\lambda_n\}_{n=1}^{\infty}$, with associated eigenfunctions $\{\varphi_n\}_{n=1}^{\infty}$ that form a basis of $\mathrm{L}^2(\mathbb{T}^2)$. Thus, we can expand $f$ and $u$ as:

$$f(x) = \sum_{n=1}^{\infty} c_n \varphi_n(x), \quad u(x,t) = \sum_{n=1}^{\infty} \alpha_n(t)\varphi_n(x), \tag{4.4}$$

for $x \in \mathbb{T}^2$ and $t \in (0,\infty)$. Here, $c_n \in \mathbb{C}$ are known and $\alpha_n$ are time-dependent coefficients that, for each $n \geq 1$, satisfy the initial-value problem (IVP):

$$i\alpha_n'(t) - \lambda_n \alpha_n = c_n e^{-i\omega_0 t}, \quad t \in (0,\infty); \quad \alpha_n(0) = 0.$$

Assuming that $\omega_0$ is not an eigenvalue of the Laplacian, we can solve this IVP and plug the resulting expression for $\alpha$ back into (4.4) to obtain:

$$u(x,t) = \sum_{n=1}^{\infty} \frac{c_n}{\omega_0 - \lambda_n} \left(e^{-i\omega_0 t} - e^{-i\lambda_n t}\right) \varphi_n(x), \quad x \in \mathbb{T}^2,\ t \in [0,\infty).$$

Similarly, if $\omega_0$ happens to be an eigenvalue of $P$, we obtain:

$$u(x,t) = \sum_{n=1}^{\infty} -ic_n\, t\, e^{-i\lambda_n t}\, \varphi_n(x), \quad x \in \mathbb{T}^2,\ t \in [0,\infty).$$

In any case, this shows that the eigenfunctions of the operator $-\Delta$ lead to a complete description of the solution to the problem (4.3).

Going back to the evolution problem (4.2), we now find ourselves in the case where $P$ (given by (4.1)) is not an elliptic operator. Moreover, because $P$ has at most a finite number of eigenvalues (cf. Theorem 3.1), their associated eigenfunctions cannot form a basis of $\mathrm{L}^2(\mathbb{T}^2)$. Consequently, it is neither immediate nor obvious that the eigenfunctions of this self-adjoint zeroth-order pseudo-differential could possibly describe the solution to the corresponding evolution problem. The following analysis will therefore focus on showing that this relationship does exist, from a numerical analysis perspective. However, we will see that some aspects from the microlocal-analysis description of the dynamics will arise in the numerical experiments, so we begin mentioning these ideas in a way that can help us better understand the outcomes.

## 4.1 Analytical description of the dynamics

The geometrical properties of the energy surface $\Sigma$ (using the terminology from [8]) on which the dynamics take place play a fundamental role in explaining key results such as Theorem 2.9 and Lemma 3.1. Because this surface depends strongly on which $r$ and $\beta$ we choose in (4.1), we consider necessary to provide a description of $\Sigma$ in a way that can be relatable to the numerical results.

Aiming at having a clearer picture of the behaviour of symbols $p = p(x,\xi)$ as $\xi \to \infty$, Dyatlov & Zworski [17] consider them as functions on the *fibre-radially compactified* cotangent bundle $\overline{T}^*\,\mathbb{T}^2$. More precisely, let $T^*\,\mathbb{T}^2 \subset (\mathbb{T}^2 \times \mathbb{R}^2)^* \simeq \mathbb{T}^2 \times \mathbb{R}^2$ denote the traditional cotangent bundle of $\mathbb{T}^2$, on which we identify $(x,\xi)$ as a coordinate system. According to [16, §E.1.3], the bundle $\overline{T}^*\,\mathbb{T}^2$ is a manifold with interior $T^*\,\mathbb{T}^2$ and boundary $\partial\overline{T}^*\,\mathbb{T}^2$, where the latter can be described as follows. First, consider an equivalence relation on $\mathbb{T}^2 \times (\mathbb{R}^2 \backslash \{0\})$ such that:

$$(x,\xi) \sim (y,\phi) \quad \Longleftrightarrow \quad x = y \quad \text{and} \quad \xi = s\phi \ \text{ for some } s > 0.$$

Then, $\partial\overline{T}^*\,\mathbb{T}^2$ is the set of equivalence classes that arise from this relation. The natural quotient map is

$$\kappa : T^*\,\mathbb{T}^2\backslash\{0\} \to \partial\overline{T}^*\,\mathbb{T}^2,$$

defined as follows: for each $(x,\xi) \in T^*\,\mathbb{T}^2\backslash\{0\}$, the ray $\{(x, s\xi)\,|\,s>0\}$ intersects $\partial\overline{T}^*\,\mathbb{T}^2$ at $\kappa(x,\xi)$, that is

$$\lim_{s\to\infty}(x, s\xi) = \kappa(x,\xi) \in \partial\overline{T}^*\,\mathbb{T}^2.$$

In this setting, Dyatlov & Zworski [17] consider that the dynamics of the problem are then dictated by the flow of

$$X := \kappa_*(|\xi|H_p) \quad \text{on} \quad \Sigma(\omega_0) := \kappa(p^{-1}(\{\omega_0\})). \tag{4.5}$$

Here, $p$ is the *principal* symbol (not to be confused with the standard symbol) of the operator $P$ defined in (4.1), that is

$$p(x,\xi) = \frac{\xi_2}{|\xi|} - r\beta(x), \quad (x,\xi) \in \overline{T}^*\,\mathbb{T}^2. \tag{4.6}$$

Also, $\kappa_*$ denotes the pushforward operator along $|\xi|H_p$ (cf. [16, §B.2]) and $|\xi|H_p$ is the (rescaled) Hamiltonian field given by:

$$|\xi|H_p = -\frac{\xi_1\xi_2}{|\xi|^2}\partial_{x_1} + \frac{\xi_1^2}{|\xi|^2}\partial_{x_2} - r\partial_{x_1}\beta|\xi|\partial_{\xi_1} - r\partial_{x_2}\beta|\xi|\partial_{\xi_2}. \tag{4.7}$$

**Example 4.1.** *Following techniques presented in [16, §E.4.3], we can obtain more information on where the attractors will form, at least for simple cases. Consider, for instance, $r>0$, $\beta(x)=\cos(x_1)$ and $\omega_0 = 0$. According to* (4.7)*, the dynamical equations are*

$$\begin{cases} \dfrac{dx_1}{dt} = -r|\xi|\sin(x_1), & \dfrac{dx_2}{dt} = 0, \\ \dfrac{d\xi_1}{dt} = \dfrac{\xi_1\xi_2}{|\xi|^2}, & \dfrac{d\xi_2}{dt} = -\dfrac{\xi_1^2}{|\xi|^2}. \end{cases} \tag{4.8}$$

*Since the energy surface $\Sigma_0$ takes the form*

$$\Sigma_0 = \kappa\left(\left\{(x_1,x_2,\xi_1,\xi_2) \in \overline{T}^*\mathbb{T}^2\backslash\{0\} : \frac{\xi_2}{|\xi|} = r\cos(x_1)\right\}\right), \tag{4.9}$$

*the system* (4.8) *restricted to $\Sigma_0$ yields*

$$\begin{cases} \dfrac{dx_1}{dt} = -r|\xi|\sin(x_1), & \dfrac{dx_2}{dt} = 0, \\ \dfrac{d\xi_1}{dt} = r\dfrac{\xi_1}{|\xi|}\cos(x_1), & \dfrac{d\xi_2}{dt} = -\dfrac{\xi_1^2}{|\xi|^2}. \end{cases} \tag{4.10}$$

*Here, we see that* $\frac{d\xi_2}{dt} < 0$*, so* $\xi_2$ *must be decreasing as* $t \to +\infty$*. Given that* $|\xi|$ *is constant (thanks to the fibre-compatification), and assuming that* $|\xi_1| > |\xi_2|$*, we must have that* $\xi_2 \to 0$*. This, in turn, implies that* $r\cos(x_1) \to 0$ *(using* (4.9)*). Since* $r > 0$*, this means that* $x_1 \to \frac{\pi}{2}$ *or* $x_1 \to -\frac{\pi}{2}$*.*

*To complete the description of the set of attracting Lagrangians* $\Lambda_0^+$*, we have to figure out the behaviour of* $\xi_1$*. Notice that, as* $\xi_2 \to 0$*,* $|\xi_1|$ *increases, and therefore, if* $\xi_1 < 0$*, we will need* $\frac{d\xi_1}{dt} < 0$*, and if* $\xi_1 > 0$ *we will need* $\frac{d\xi_1}{dt} > 0$*. First, linearizing* (4.10) *around* $x_1 = \pi/2$*,* $x_2 \in \mathbb{S}^1$*,* $\xi_2 = 0$*, we notice that* $\xi_1$ *must be negative in order to get a sink of the dynamical system. Similarly, linearizing around* $x_1 = -\pi/2$*,* $x_2 \in \mathbb{S}^1$ *and* $\xi_2 = 0$*, we have that* $\xi_1$ *must be positive to get a source of the system. Therefore,*

$$\Lambda_0^+ = \left\{x_1 = \frac{\pi}{2},\ x_2 \in \mathbb{S}^1,\ \xi_1 < 0,\ \xi_2 = 0\right\} \cup \left\{x_1 = -\frac{\pi}{2},\ x_2 \in \mathbb{S}^1,\ \xi_1 > 0,\ \xi_2 = 0\right\}. \quad (4.11)$$

The long-term evolution described by Theorem 2.9 is first given in the work by Colin de Verdière & Saint-Raymond [9]. Here, two of the main assumptions are

1. The flow of $X$ on $\Sigma$ is Morse-Smale (cf. Appendix A) with no fixed points. By the Poincaré-Bendixon theorem (cf., e.g., [31, 41]), this forces $\Sigma$ to be a finite union of tori.

2. The energy surface $\Sigma$ covers $\mathbb{T}^2$.

Although the latter has been relaxed in later works (see [8, 17]), we believe that a lose of this property may change the behaviour of the solution in a noticeable way. First, for the case $\omega_0 = 0$, we notice from (4.6) that

$$p(x,\xi) = 0 \quad \Longleftrightarrow \quad r\beta(x) = \frac{\xi_2}{|\xi|}, \quad (4.12)$$

but because $(x,\xi) \in \overline{T}^*\,\mathbb{T}^2$, we may parametrize $\xi$ as $(s\cos(\eta), s\sin(\eta))$ for $\eta \in [-\pi,\pi)$ and some $s > 0$. Replacing this into (4.12) leads to a more familiar characterization of the energy surface $\Sigma$:

$$\Sigma = \Big\{(x_1,x_2,\eta) \in \mathbb{T}^3 :\ r\,\beta(x_1,x_2) = \sin(\eta)\Big\}, \quad (4.13)$$

where $\mathbb{T}^3$ is the standard 3-torus. Hence, $\Sigma$ will not cover $\mathbb{T}^2$ if and only if there exists $x = (x_1,x_2) \in \mathbb{T}^2$ such that for any $\eta \in \mathbb{S}^1$, the equation $r\beta(x) = \sin(\eta)$ does not have a solution.

## 4.2 Numerical results

Because the eigenvalues of $P$ are embedded in a continuous spectrum (cf. Theorem 3.1), they cannot be computable in an explicit way (and neither can the eigenfunctions of $P$).

Therefore, we will resort to the viscous limit of this operator (i.e. $P + i\nu\Delta$ and the eigenvalue problem (3.4)) and the techniques described in Section 3.3 for the computation of its spectrum. Furthermore, we will focus on those eigenvalues near the origin, as per Theorem 3.2. We compute the eigenvalues of $P + i\nu\Delta$ for different viscosities, and then we analyze the regularity of these eigenfunctions. Then, we have a look at how these low-viscosity eigenfunctions relate to the development of attractors in the evolution problem (2.5). The following sets of data will henceforth be used:

**Test 1:** $r = 0.5$, $\beta(x) = \cos(x_1)$ and $\nu \in [2.3, 9.3] \cdot 10^{-3}$.

**Test 2:** $r = 0.5$, $\beta(x) = \cos(x_1) + \sin(x_2)$ and $\nu \in [1.3, 9.3] \cdot 10^{-3}$.

**Test 3:** $r = 0.45$, $\beta(x) = \cos(x_1 - 2x_2) + \sin(2x_2)$ and $\nu \in [3 \cdot 10^{-4}, 10^{-2}]$.

**Test 4:** $r = 0.55$, $\beta(x) = \cos(x_1 - 2x_2) + \sin(2x_2)$ and $\nu \in [3 \cdot 10^{-4}, 10^{-2}]$.

We have chosen these tests to show that the attractors become increasingly complex. Also, note that the difference between Tests 3 and 4 is only a slight increase in the parameter $r$. In all the experiments, the eigenvalue problem (3.4) is discretized using a mesh $\mathcal{T}_N$ with $N = 64$ grid points per direction.

### 4.2.1 Energy surfaces

For each one of the described tests, we can compute their associated energy surfaces $\Sigma_j = \kappa\left(p_j^{-1}(\{0\})\right)$. For Tests 1, 2, 3 and 4, their corresponding $\Sigma_j$ read:

$$\Sigma_1 := \Big\{(x_1, x_2, \eta) \in \mathbb{T}^3 \ : \ 0.5\cos(x_1) = \sin(\eta) \ \Big\}, \tag{4.14}$$

$$\Sigma_2 := \Big\{(x_1, x_2, \eta) \in \mathbb{T}^3 \ : \ 0.5\Big(\cos(x_1) + \sin(x_2)\Big) = \sin(\eta) \ \Big\}, \tag{4.15}$$

$$\Sigma_3 := \Big\{(x_1, x_2, \eta) \in \mathbb{T}^3 \ : \ 0.45\Big(\cos(x_1 - 2x_2) + \sin(2x_2)\Big) = \sin(\eta) \ \Big\}, \tag{4.16}$$

$$\Sigma_4 := \Big\{(x_1, x_2, \eta) \in \mathbb{T}^3 \ : \ 0.55\Big(\cos(x_1 - 2x_2) + \sin(2x_2)\Big) = \sin(\eta) \ \Big\}. \tag{4.17}$$

From Section 4.1, we obtain that $\Sigma$ will be a finite union of tori that covers $\mathbb{T}^2$ if $r|\beta(x)| \leq 1$ for any $x \in \mathbb{T}^2$. This is the case for $\Sigma_j$, $j \in \{1, 2, 3\}$, but not for $\Sigma_4$, since there are values of $x \in \mathbb{T}^2$ for which no $\eta$ satisfies the equation $0.55\Big(\cos(x_1 - 2x_2) + \sin(2x_2)\Big) = \sin(\eta)$. To portray this, we pick an appropriate level curve in each $\Sigma_j$, which we show in Figure 4.1. Fortunately, these surfaces are not too complicated to visualize them as a whole, so we also offer this view in Figures 4.2 and 4.3.

### 4.2.2 Resonances near the origin

For Tests 1 and 2, we compute the first 8 eigenvalues of the operator $P + i\nu\Delta$ for values of $\nu$ within the previously specified ranges, whereas for Tests 3 and 4 we compute the first 7 eigenvalues. We portray these results in Figures 4.4-4.7.

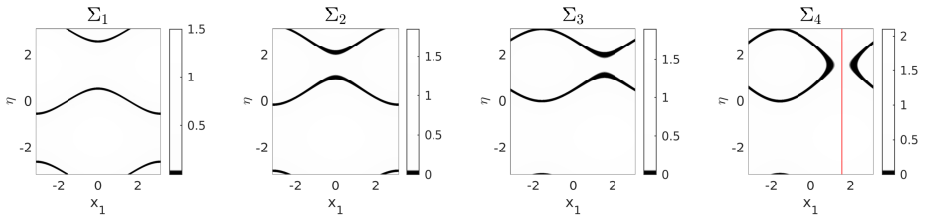


Figure 4.1: Level curves $x_2 = \pi/4$ of the different $\Sigma_j$ defined in (4.14)-(4.17). Here we only plot those values $(x_1, \eta)$ for which $|r\beta(x) - \sin(\eta)| = 0$. For $\Sigma_4$, the red line is located at $x_1 = \pi/2$ and denotes points for which no value of $\eta$ satisfy the previous equation, hence, this surface will not cover $\mathbb{T}^2$.

Overall, the eigenvalues are located in the lower half of the complex plane, and these move upwards toward the real axis as $\nu \to 0^+$. This is expected since $i\nu\Delta$ is a second-order differential operator with a purely complex spectrum that lies on the negative part of the imaginary axis. However, as pointed out in Section 3.2, in the limit there might be some eigenvalues that will stay below the real axis (recall that $P + i\nu\Delta$ is not a self-adjoint operator and that $\sigma(P + i\nu\Delta) \not\to \sigma(P)$ as $\nu \to 0^+$).

Notice that the ordering of these eigenvalues works well for Tests 1 and 2 in the sense that we are able to track important trajectories (such as ones drawn by the first and fifth eigenvalues). Furthermore, we confirm that the trajectories are $C^\infty$ curves, as recently shown by Wang [44]. We also see that there is an observed symmetry with respect to the imaginary axis. Figures 4.4 and 4.5 suggest that if $\lambda^{(\nu)}$ is an eigenvalue, then so is $-\overline{\lambda^{(\nu)}}$. However, the situation is different in Tests 3 and 4.

First, we see in Figure 4.6 that $\lambda_1^{(\nu)}$ is an simple eigenvalue moving along the real axis. Moreover, in Test 4 (see Figure 4.7), $\lambda_2^{(\nu)}$ and $\lambda_5^{(\nu)}$ appear in pairs (as before) but only below $\nu = 4.4 \cdot 10^{-3}$. Therefore, for these particular cases, we have ordered the eigenvalues in a "magnitude-then-phase" way first (described in Section 3.5), and then used the following order: first those eigenvalues $\lambda$ with $|\operatorname{Re}(\lambda)| <= 0.5 \cdot 10^{-3}$, then those with $\operatorname{Re}(\lambda) > 0.5 \cdot 10^{-3}$ and finally those with $\operatorname{Re}(\lambda) < -0.5 \cdot 10^{-3}$.

One additional thing to notice in Tests 3 and 4 is how all seven computed eigenvalues move toward a neighbourhood of 0 as $\nu \to 0^+$, in comparison to Tests 1 and 2 where some eigenvalues appear to be moving toward the real axis, but not toward 0. We conjecture that the difference in these cases is due to the presence of an eigenvalue at 0 in Tests 3 and 4, but not in Tests 1 and 2.

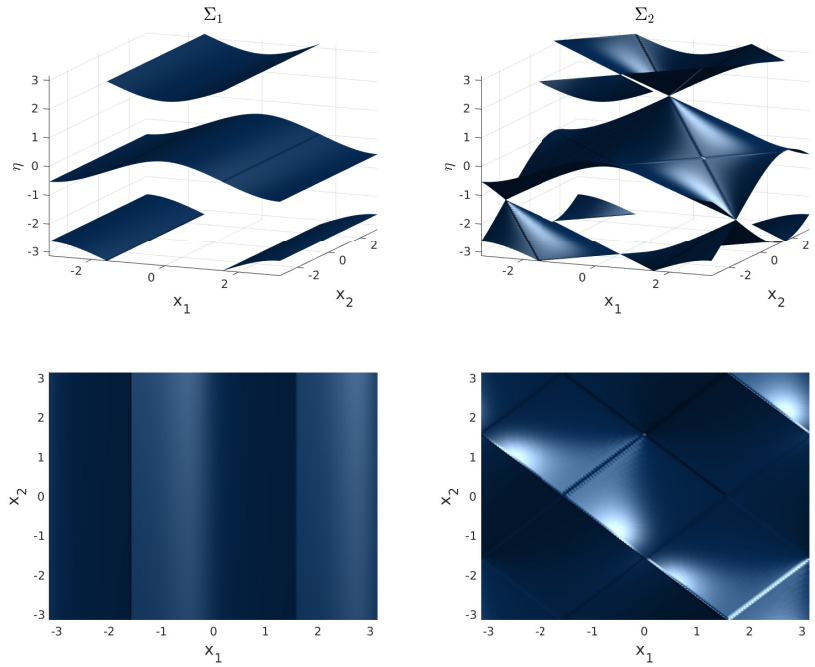


Figure 4.2: Energy surfaces $\Sigma_1$ and $\Sigma_2$ when viewed from an angle (top) and from the top (bottom). The latter shows that the energy shell do cover $\mathbb{T}^2$.

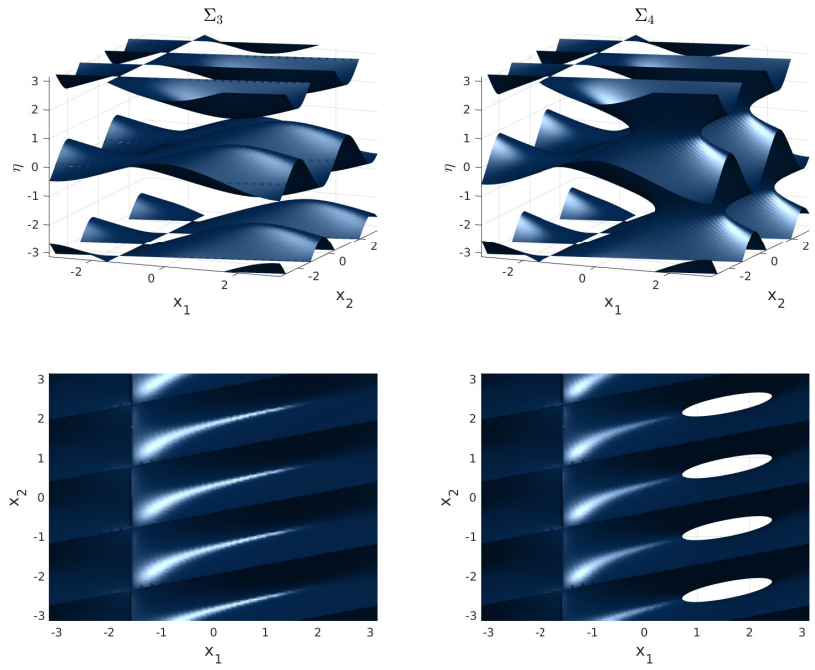


Figure 4.3: Energy surfaces $\Sigma_3$ and $\Sigma_4$ when viewed from an angle (top) and from the top (bottom). In particular, the holes in the bottom-right plot show that $\Sigma_4$ does not cover $\mathbb{T}^2$.

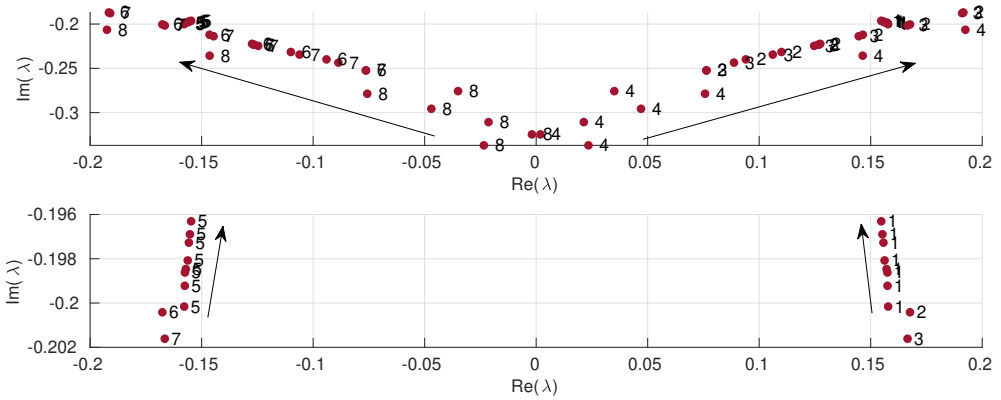


Figure 4.4: Evolution of the first 8 eigenvalues in Test 1 ($r = 0.5$, $\beta(x) = \cos(x_1)$) as $\nu$ decreases. While some of them move in an oblique direction away from 0 (top), a closer look near the points $\pm 0.15 - 0.2i$ (bottom) shows that the first and fifth eigenvalues are moving slowly upwards.

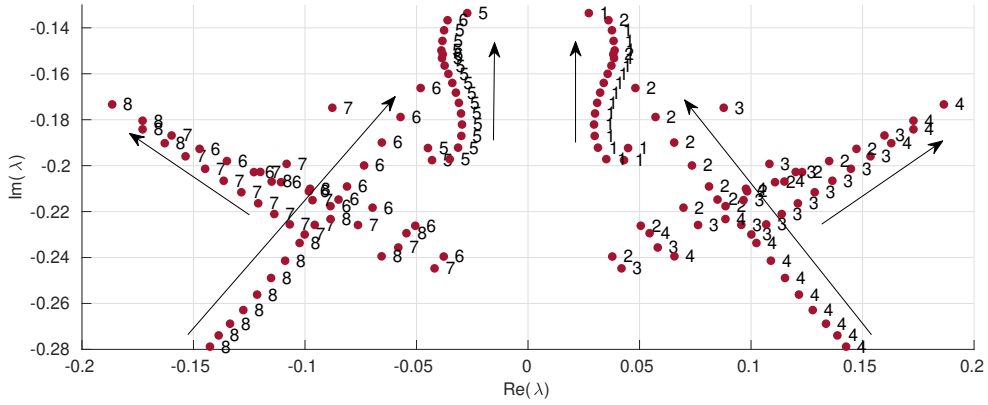


Figure 4.5: Evolution of the first 8 eigenvalues in Test 2 ($r = 0.5$, $\beta(x) = \cos(x_1) + \sin(x_2)$) as $\nu$ decreases. Here, the first, fifth, second and sixth eigenvalues (fourth and eighth, respectively, for higher viscosities) appear to be moving toward a neighbourhood of 0 (in the direction of the arrows).

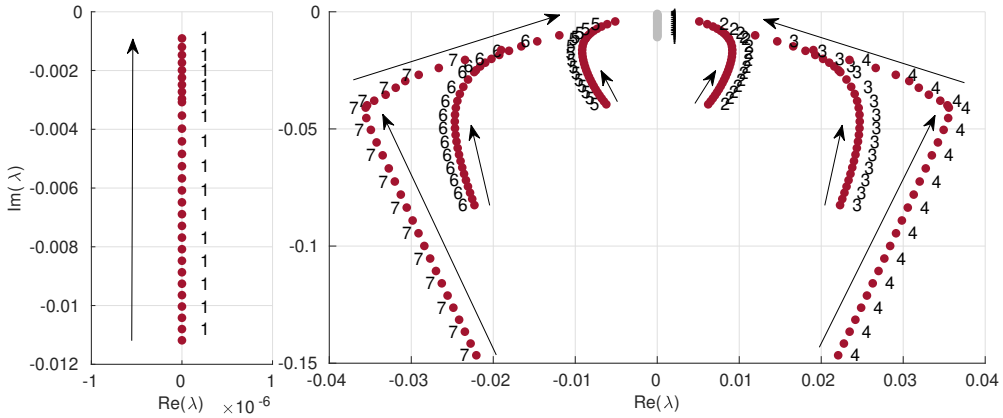


Figure 4.6: Evolution of the first eigenvalue (left) and second to seventh eigenvalues (right) for Test 3 ($r = 0.45$, $\beta(x) = \cos(x_1 - 2x_2) + \sin(x_2)$) when the viscosity decreases from $10^{-2}$ to $3 \cdot 10^{-4}$.

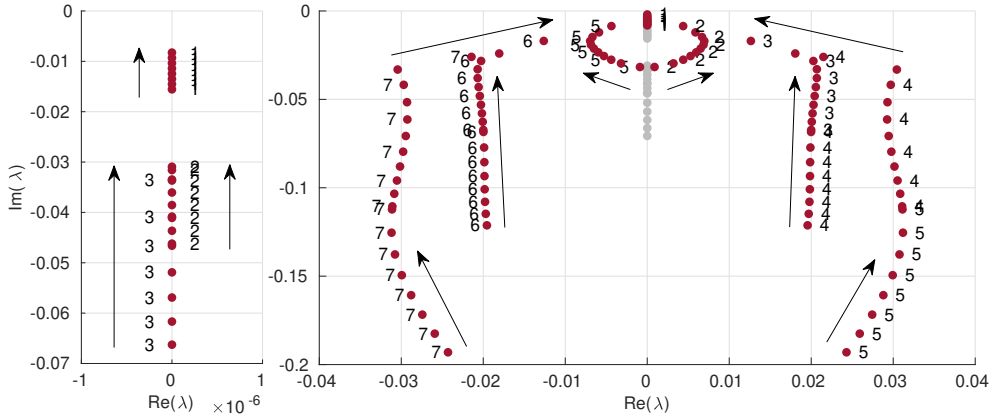


Figure 4.7: Evolution of the first seven eigenvalues for Test 4 ($r = 0.55$, $\beta(x) = \cos(x_1 - 2x_2) + \sin(x_2)$). Left: first three eigenvalues when the viscosity decreases from $10^{-2}$ to $4.4 \cdot 10^{-3}$ (below this viscosity, these eigenvalues become the first, second and fifth eigenvalues, respectively). Right: all seven eigenvalues as $\nu$ decreases from $10^{-2}$ to $3 \cdot 10^{-4}$.

### 4.2.3 Regularity of eigenmodes

To get more information on the smoothness of some of the eigenmodes corresponding to $P + i\nu\Delta$, we have computed their radial energy density $E_0$ for the different viscosities considered in Figures 4.4-4.7, with the focus mainly on those related to eigenvalues that appear to be moving to 0 (bearing in mind Theorem 3.2). These results are portrayed in Figures 4.8, 4.9 and 4.10 and 4.11, respectively for Tests 1, 2, 3 and 4.

Overall, the Fourier coefficients appear to decay quickly, which suggests the corresponding eigenmodes live in the smoother part of the inclusion (3.7), that is,

$$\mathscr{A}_{\widetilde{\delta}} \subset \mathcal{X} \subset \mathscr{A}_{-\widetilde{\delta}}.$$

In addition, we notice how an increase in $r$ from 0.45 in Test 3 to 0.55 in Test 4 makes the Fourier coefficients of eigenfunctions decay slightly slower. This decrease in regularity may potentially be attributed to the fact that, for the choices in Test 4, the energy surface $\Sigma_4$ does not cover $\mathbb{T}^2$ (see Section 4.2.1).

### 4.2.4 Low-viscosity eigenmodes and long-term behaviour

We would like now to visualize how low-viscosity eigenmodes may influence the long-time evolution of the transient solutions of (2.5). One important thing to notice first is that the geometric structure of the attractors is independent of the forcing term $f$. Indeed, when $\beta(x) = \cos(x_1)$, the set of attracting Lagrangians is given by (4.11) regardless of the source term $f$. We can numerically verify this claim for this particular case. Indeed, we perform a simple experiment using $r = 2$ and the aforementioned $\beta$, and we show the results in Figure 4.12. Here, we see that depending on the structure of the forcing function, the attractors appear with different intensities but with the same shape. Therefore, in all the subsequent experiments, we consider a centred Gaussian as forcing function for the evolution problem, with a forcing frequency $\omega_0 = 0$.

Let us have a look at some the viscous eigenmodes in (3.4) corresponding to the eigenvalues closest to 0, with the viscosity taken as the smallest ones considered in Section 4.2.2. We can then make the comparison with the long-term evolution of the solution to (2.5).

First, using the parameters from Test 1, we see in Figure 4.13 how the first and fifth eigenmodes match the shape and location of the attractors (see (4.11)). Moreover, according to Figure 4.14, these eigenmodes capture some of the energy content of the transient solution. Then, we can see similar situations using the parameters from Test 2, 3 and 4 (see Figures 4.15, 4.17 and 4.19, respectively) where different eigenmodes capture different parts of the attractors.

In turn, the magnitude of the Fourier coefficients of these modes seems also to provide some information about the where the wave energy is concentrated in the transient solution (see Figures 4.16, 4.18 and 4.20). Additionally, by looking at these eigenmodes in Fourier

space, we can corroborate the smoothness that the radial energy density $E_0$ suggests (discussed in the previous sections). In particular, the eigenmodes in Tests 1, 2 and 3 seem to be compactly supported, whereas for Test 4, while the frequencies are more spread out, the highest amplitudes are still concentrated in the center of the spectrum. This also shows the sensitivity of the transient solution (and consequently, of the eigenmodes) with respect to the parameter $r$, since a small increase from $r = 0.45$ to $r = 0.55$ changes most of the structure of the attractors. Indeed, as the projection of the attracting Lagrangian under the map $\kappa$ is a subset of the energy shell $\Sigma$ (cf. [17]), the appearance of holes in $\Sigma$ (see Figure 4.3 bottom-right) will necessarily modify the structure of the attractors.

As a final note, we can also observe from Figures 4.13-4.20 how the numerics reveal the contrasting character between the smoothness of the embedded eigenmodes (which are analytic) and that of the long-term evolution (which is not square-integrable). Indeed, the additional presence of a continuous spectrum is fundamental to explain this discrepancy.

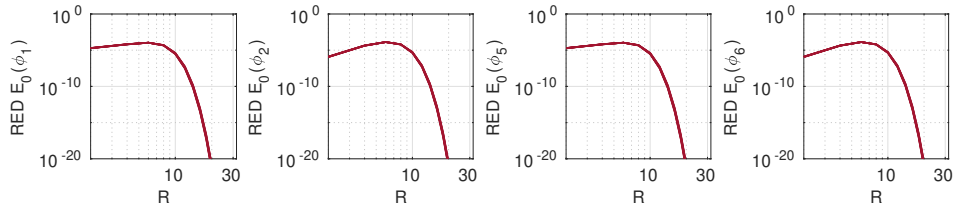


Figure 4.8: Radial energy density $E_0$ (log-log scale) of the first, second, fifth and sixth eigenmodes of $\langle D \rangle^{-1} D_{x_2} + i\nu\Delta - 0.5\cos(x_1)$ (Test 1) for different values of $\nu$. The curves are very close to each other and drop below machine epsilon (the vertical axis has been truncated).

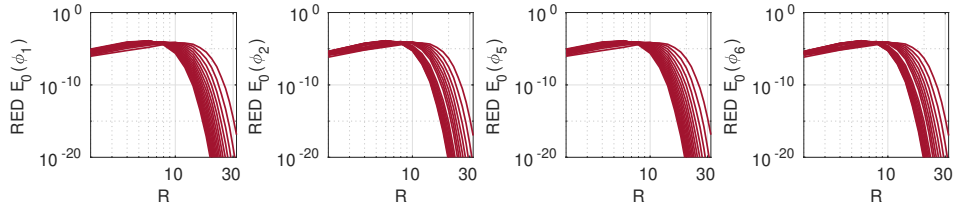


Figure 4.9: Radial energy density $E_0$ (log-log scale) of the first, second, fifth and sixth eigenmodes of $\langle D \rangle^{-1} D_{x_2} + i\nu\Delta - 0.5(\cos(x_1) + \sin(x_2))$ (Test 2) for different values of $\nu$. As the viscosity decreases, the curves move to the right (the vertical axis has been truncated).

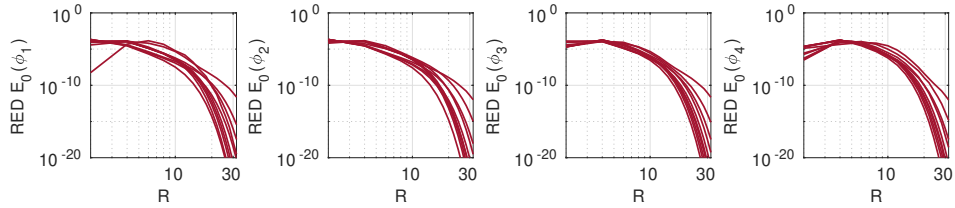


Figure 4.10: Radial energy density $E_0$ (log-log scale) of the first four eigenmodes of $\langle D \rangle^{-1} D_{x_2} + i\nu\Delta - 0.45(\cos(x_1 - 2x_2) + \sin(x_2))$ (Test 3) for different values of $\nu$. As the viscosity decreases, the curves move to the right.

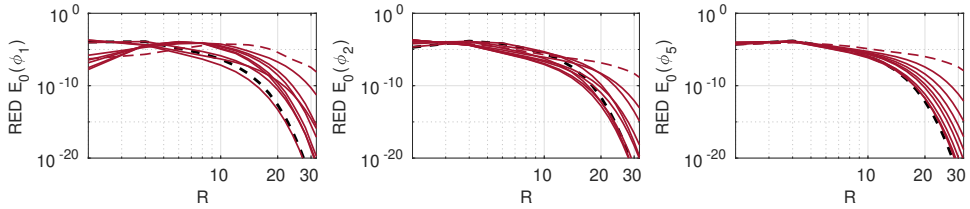


Figure 4.11: Radial energy density $E_0$ (log-log scale) of the first, second and fifth eigenmodes of $\langle D \rangle^{-1} D_{x_2} + i\nu\Delta - 0.55(\cos(x_1 - 2x_2) + \sin(x_2))$ (Test 4) for different values of $\nu$. The dashed curve in black corresponds to the largest viscosity considered ($\nu = 10^{-2}$), while the dashed curve in red corresponds to the smallest one ($\nu = 3 \cdot 10^{-4}$).

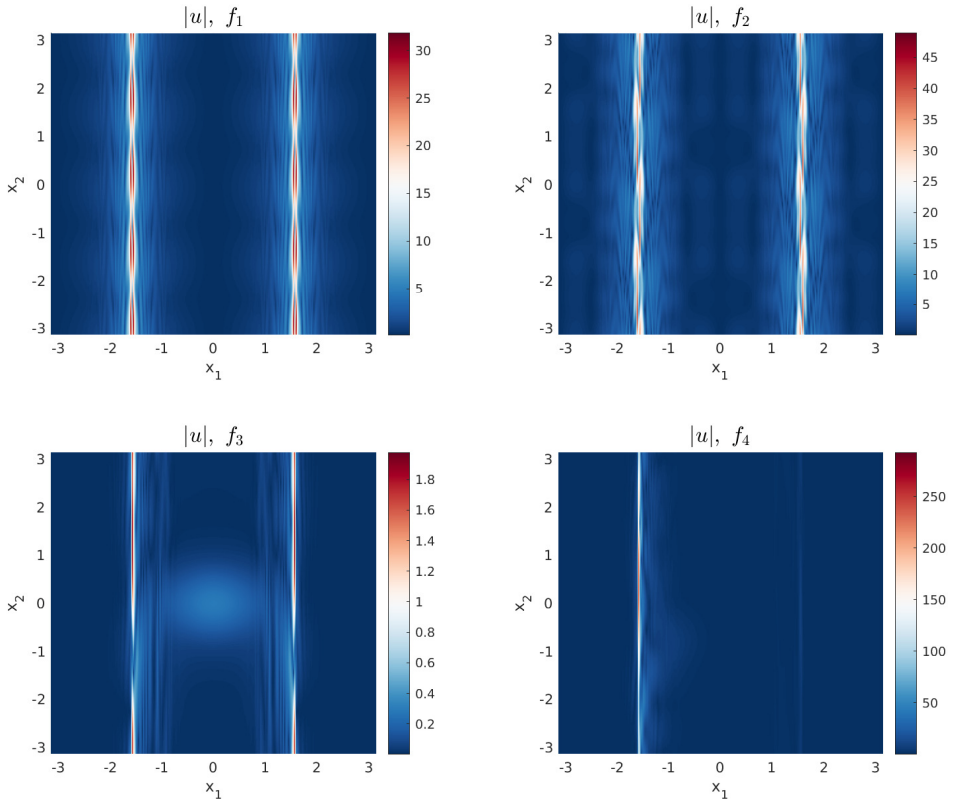


Figure 4.12: Solution to the evolution problem (4.2) at time $t = 1000$ with $r = 2$, $\beta(x) = \cos(x_1)$, $\omega_0 = 0$ and the following forcing terms: $f(x) = \sin(x_1)\cos(2x_2)$ (top left), $f(x) = \sin(x_1)\cos(2x_2) + \sin(5x_1)\cos(2x_2) + i\sin(5x_1)\cos(4x_2)$ (top right), $f(x) = 0.5\exp(-2|x|^2)$ (bottom left) and $f(x) = -5\exp(-3((x_1+0.9)^2+(x_2+0.8)^2)+i(2x_1+x_2))$ (bottom right). Approximations computed using $N = 256$ grid points per direction and $\Delta t = 0.5$.

.

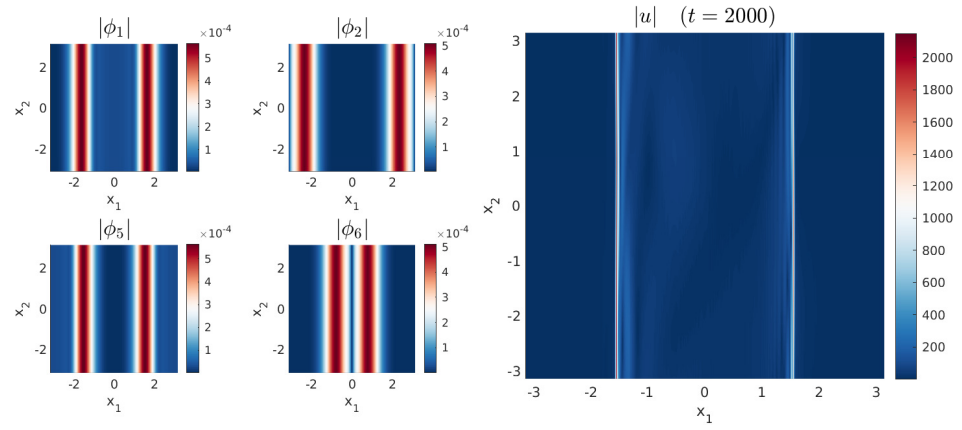


Figure 4.13: Left half: first, second, fifth and sixth eigenmodes of $\langle D \rangle^{-1} D_{x_2} + i\nu\Delta - 0.5\cos(x_1)$ (Test 1) with $\nu = 2.3 \cdot 10^{-3}$. Right half: solution to the evolution problem (4.2) at time $t = 2000$ (refer to Figure 4.4 for a view of the corresponding eigenvalues and to Figure 4.8 for plots of the RED).

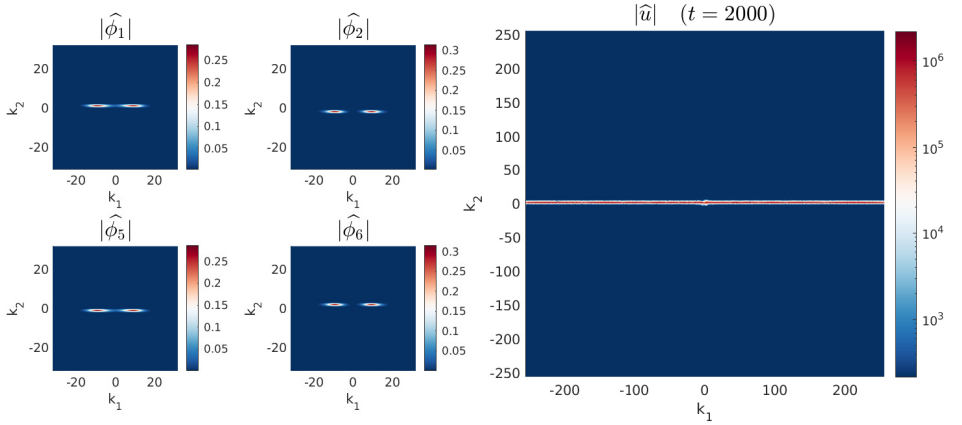


Figure 4.14: Left half: magnitude of the Fourier coefficients of the first, second, fifth and sixth eigenmodes of $\langle D \rangle^{-1} D_{x_2} + i\nu\Delta - 0.5\cos(x_1)$ (Test 1) with $\nu = 2.3 \cdot 10^{-3}$. Right half: magnitude of the Fourier coefficients of the solution to the evolution problem at time $t = 2000$

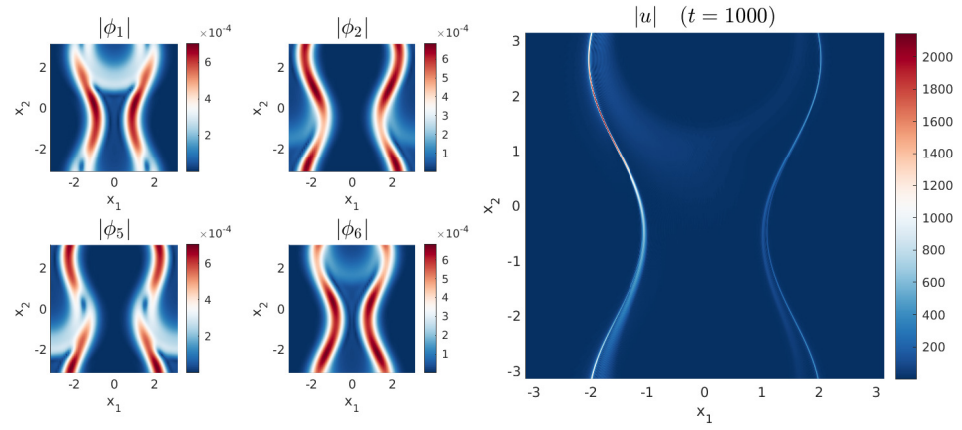


Figure 4.15: Left half: first, second, fifth and sixth eigenmodes of $\langle D \rangle^{-1} D_{x_2} + i\nu\Delta - 0.5(\cos(x_1) + \sin(x_2))$ (Test 2) with $\nu = 1.3 \cdot 10^{-3}$. Right half: solution to the evolution problem (4.2) at time $t = 1000$ (refer to Figure 4.5 for a view of the corresponding eigenvalues and to Figure 4.9 for plots of the RED).

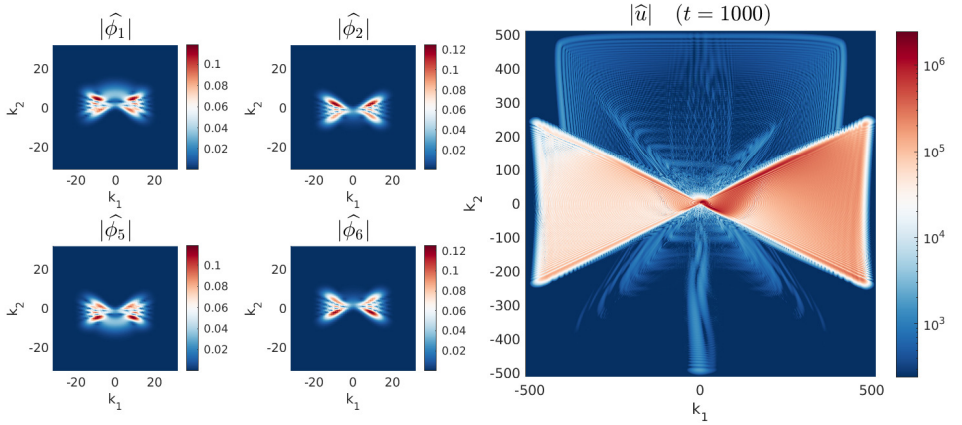


Figure 4.16: Left half: magnitude of the Fourier coefficients of the first, second, fifth and sixth eigenmodes of $\langle D \rangle^{-1} D_{x_2} + i\nu\Delta - 0.5(\cos(x_1) + \sin(x_2))$ (Test 2) with $\nu = 1.3 \cdot 10^{-3}$. Right half: magnitude of the Fourier coefficients of the solution to the evolution problem at time $t = 1000$.

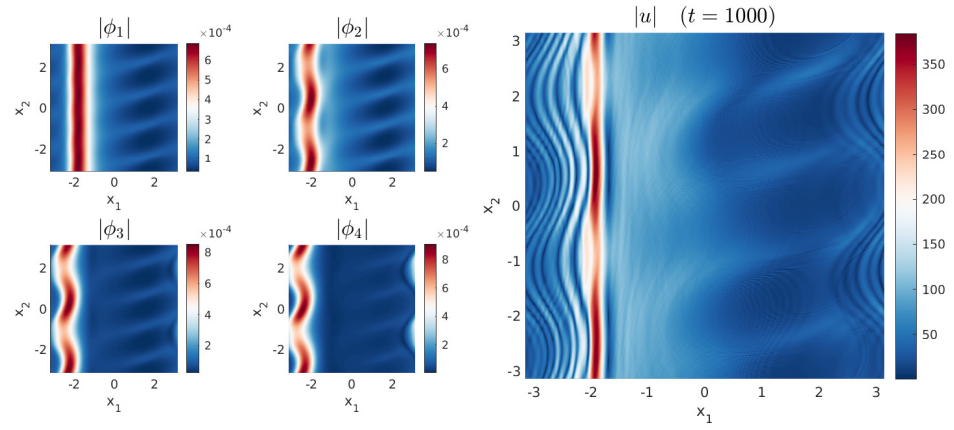


Figure 4.17: Left half: first four eigenmodes of $\langle D \rangle^{-1} D_{x_2} + i\nu\Delta - 0.45(\cos(x_1 - 2x_2) + \sin(x_2))$ (Test 3) with $\nu = 3.0 \cdot 10^{-4}$. Right half: solution to the evolution problem (4.2) at time $t = 1000$ (refer to Figure 4.6 for a view of the corresponding eigenvalues and to Figure 4.10 for plots of the RED).

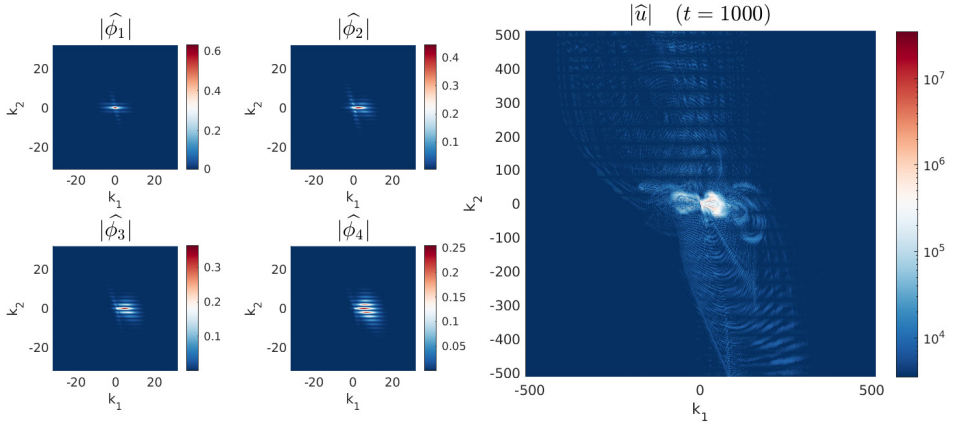


Figure 4.18: Left half: magnitude of the Fourier coefficients of the first four eigenmodes of $\langle D \rangle^{-1} D_{x_2} + i\nu\Delta - 0.45(\cos(x_1 - 2x_2) + \sin(x_2))$ (Test 3) with $\nu = 3.0 \cdot 10^{-4}$. Right half: magnitude of the Fourier coefficients of the solution to the evolution problem at time $t = 1000$.

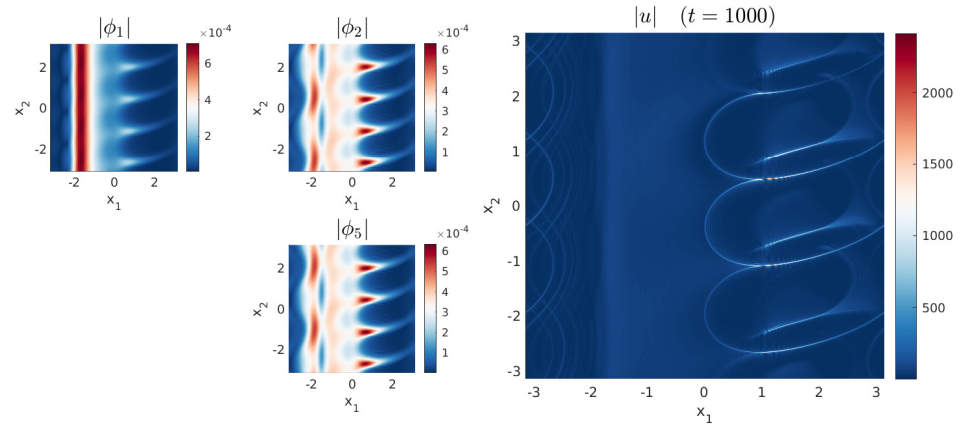


Figure 4.19: Left half: first, second and fifth eigenmodes of $\langle D \rangle^{-1} D_{x_2} + i\nu\Delta - 0.55(\cos(x_1 - 2x_2) + \sin(x_2))$ (Test 4) with $\nu = 3.0 \cdot 10^{-4}$. Right half: solution to the evolution problem (4.2) at time $t = 1000$ (refer to Figure 4.7 for a view of the corresponding eigenvalues and to Figure 4.11 for plots of the RED).

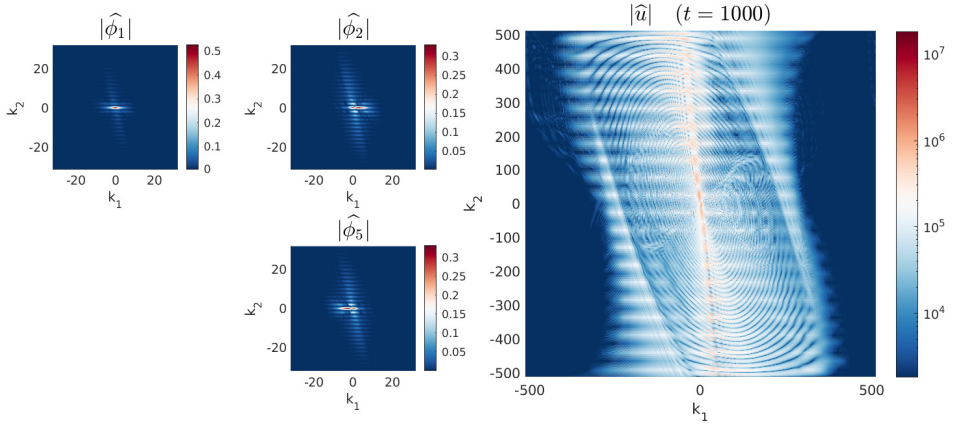


Figure 4.20: Left half: magnitude of the Fourier coefficients of the first, second and fifth eigenmodes of $\langle D \rangle^{-1} D_{x_2} + i\nu\Delta - 0.55(\cos(x_1 - 2x_2) + \sin(x_2))$ (Test 4) with $\nu = 3.0 \cdot 10^{-4}$. Right half: magnitude of the Fourier coefficients of the solution to the evolution problem at time $t = 1000$.

# Chapter 5

# Conclusions and Future Work

## 5.1 Conclusions

In this thesis, we developed numerical algorithms for, and performed a computational study of, the relationship between internal wave attractors and the spectra of a class of zeroth-order pseudo-differential operators.

In Chapter 2, we developed a numerical method to approximate the solution to the nonlocal, linear forced wave equation (2.5) in the standard 2-torus. The construction was based on the coupling of a high-order time-stepping method with a fast pseudo-spectral discretization in the spatial variables. The numerical results show that the methods are fourth-order-in-time accurate, and locally spectrally accurate in space. We cannot expect global-in-space accuracy due to the singularity brought by the attractors. On the other hand, an analysis in Fourier space allows us to show that the method captures the main physical and analytical aspects of flow, such as the non-square-integrability for long times and the linear evolution of the squared $\mathrm{L}^2$-norm of the solution.

In Chapter 3, we turned our attention to the numerical approximation of the embedded eigenvalues of the wave operator, by means of a viscous approximation. Here, the natural application of the discrete Fourier transform in a pseudo-spectral fashion leads to a non-Hermitian, full matrix, which is very sensitive to round-off errors. Nevertheless, the use of an Arnoldi-type iteration leads to eigenvalues that are computed with spectral accuracy.

Finally, the methods developed for the evolution and eigenvalue problems are used together to analyze further spectral properties of the pseudo-differential operator. Firstly, we showed that a novel proposed sorting method for the eigenvalues effectively captures $C^\infty$ trajectories that approximate the embedded eigenvalues as the viscosity decreases. Secondly, we explored how some of the viscous eigenmodes become slightly less smooth as the viscosity decreases. Lastly, we explored the effect of the embedded eigenmodes in the long-term dynamics of the flow. We compared side-by-side low-viscosity eigenmodes and the evolution (both in real and frequency space) and related some of the observed behaviour to the geometrical structure of the energy surfaces on which the flow takes places. We conclude

that the embdedded eigenmodes describe (at least, partially) the long-term dynamics of the problem.

## 5.2 Future work

The microlocal analysis of internal waves is a very new area of research, and therefore, there are many directions in which the work presented here can continue from a numerical perspective:

1. The description in Fourier space of the nonlocal wave operator provides a straightforward way to apply pseudo-spectral methods. Nevertheless, the evolution problem in Fourier space (2.16) could also be discretized using pure spectral methods, finite differences or finite element methods (to name a few). However, they would need to address the computation of the convolution in an efficient way.

2. The discretization techniques used throughout Chapters 2 and 3 could also be used for more involved versions of the operator $P$, such as those found in [18, 42, 44].

3. As we saw in Section 3.4, the solution to the eigenvalue problem by means of the two-dimensional discrete Fourier transform (DFT) is computationally very expensive (even when using an FFT-based algortihm) due to fill-in. Therefore, more efficient implementations of the DFT are needed in order to preserve the sparsity of the matrix.

4. De-aliasing techniques were not considered in this work. On the one hand, it is known that pseudo-spectral methods amplify aliasing errors when the solution lacks regularity. On the other hand, standard tools such as the two-thirds rule or spectral viscosity methods (cf. [3]) may not be the best alternative for this problem. Indeed, the high frequencies are key to describe the singularity of the solution, and removing them without careful thought could lead to an unrealistic smoothing of the dynamics. Thus, it still remains to determine a proper de-aliasing strategy for this problem.

As the results in this thesis suggest, both the spectral and dynamic behaviour of PDEs with zero-order pseudo-differential operators is remarkably rich, and accurate numerical simulations can help shed insight. Carefully designed discretizations can aid analysts in the quest for new analytical results, and as such, further research in this area is encouraged.

# Bibliography


[1] W. O. Amrein. *Hilbert Space Methods in Quantum Mechanics*. Fundamental sciences. EFPL Press, 2009.

[2] X. Antoine and E. Lorin. A simple pseudospectral method for the computation of the time-dependent Dirac equation with Perfectly Matched Layers. *J. Comput. Phys.*, 395:583–601, 2019.

[3] C. Bardos and E. Tadmor. Stability and spectral convergence of Fourier method for nonlinear problems: on the shortcomings of the 2/3 de-aliasing method. *Numer. Math.*, 129(4):749–782, 2015.

[4] V. I. Bogachev. *Real and Functional Analysis*. Moscow Lectures, 4. Springer, 1st edition, 2020.

[5] C. Brouzet, I. N. Sibgatullin, H. Scolan, E. V. Ermanyuk, and T. Dauxois. Internal wave attractors examined using laboratory experiments and 3D numerical simulations. *J. Fluid Mech.*, 793:109–131, 2016.

[6] R. E. Caflisch, F. Gargano, M. Sammartino, and V. Sciacca. Complex singularities and PDEs. *Riv. Math. Univ. Parma*, 6(1):69–133, 2015.

[7] I. M. Cohen and P. K. Kundu. *Fluid Mechanics*. Elsevier Science, 3rd edition, 2004.

[8] Y. Colin de Verdère. Spectral theory of pseudo-differential operators of degree 0 and application to forced linear waves. *Anal. PDE*, 13(5):1521–1537, 2020.

[9] Y. Colin de Verdière and L. Saint-Raymond. Attractors for two dimensional waves with homogeneous Hamiltonians of degree 0. *Commun. Pure Appl. Anal.*, 2:421–462, 2020.

[10] S. M. Cox and P. C. Matthews. Exponential time differencing for stiff systems. *J. Comput. Phys.*, 176(2):430–455, 2002.

[11] G. G. Dahlquist. A special stability problem for linear multistep methods. *BIT Numer. Math.*, 3(1):27–43, 1963.

[12] N. V. Dang and G. Riviere. Spectral analysis of Morse–Smale flows I: Construction of the anisotropic spaces. *J. Inst. Math. Jussieu*, pages 1–57, 2018.

[13] G. Davis, T. Jamin, J. Deleuze, S. Joubaud, and T. Dauxois. Succession of resonances to achieve internal wave turbulence. *Phys. Rev. Lett.*, 124(20):204502, 2020.

[14] S. Drijfhout and L. R. M. Maas. Impact of channel geometry and rotation on the trapping of internal tides. *J. Phys. Oceanogr.*, 37(11):2740–2763, 2007.

[15] S. Dyatlov and M. Zworski. Stochastic stability of Pollicott–Ruelle resonances. *Nonlinearity*, 28(10):3511, 2015.

[16] S. Dyatlov and M. Zworski. *Mathematical Theory of Scattering Resonances*. Graduate Studies in Mathematics. American Mathematical Society, 2019.

[17] S. Dyatlov and M. Zworski. Microlocal analysis of forced waves. *Pure Appl. Anal.*, 1:359–384, 2019.

[18] J. Galkowski and M. Zworski. Viscosity limits for 0th order pseudodifferential operators. *arXiv e-prints*, page arXiv:1912.09840, December 2019.

[19] C. Garrett and W. Munk. Internal waves in the ocean. *Ann. Rev. Fluid Mech.*, 11(1):339–369, 1979.

[20] N. Grisouard, C. Staquet, and I. Pairaud. Numerical simulation of a two-dimensional internal wave attractor. *J. Fluid Mech.*, 614:1–14, 2008.

[21] J. K. Hale. Stability and gradient dynamical systems. *Rev. Mat. Complut.*, 17(1):7–57, 2004.

[22] J. Hazewinkel, P. Van Breevoort, S. B. Dalziel, and L. R. M. Maas. Observations on the wavenumber spectrum and evolution of an internal wave attractor. *J. Fluid Mech.*, 598:373, 2008.

[23] L. Hörmander. *The Analysis of Linear Partial Differential Operators III: Pseudo-Differential Operators*. Springer, 2007.

[24] C. Klein. Fourth order time-stepping for low dispersion Korteweg-de Vries and nonlinear Schrödinger equation. *Electron. Trans. Numer. Anal.*, 29:116–135, 2008.

[25] F.-P. A. Lam and L. R. M. Maas. Internal wave focusing revisited; a reanalysis and new theoretical links. *Fluid Dyn. Res.*, 40(2):95, 2008.

[26] M. P. Lamoureux and G. F. Margrave. An introduction to numerical methods of pseudodifferential operators. In J. Toft H. G. Feichtinger, N. Lerner, editor, *Pseudo-Differential Operators: Quantization and Signals*, chapter 3, pages 79–134. Springer, Berlin, 2008.

[27] X. Liang and A. Q. M. Khaliq. An efficient Fourier spectral exponential time differencing method for the space-fractional nonlinear Schrödinger equations. *Comput. Math. Appl.*, 75(12):4438–4457, 2018.

[28] L. R. M. Maas. Wave attractors: linear yet nonlinear. *Int. J. Bifurcat. Chaos*, 15(9):2757–2782, 2005.

[29] L. R. M. Maas, D. Benielli, J. Sommeria, and F.-P. A. Lam. Observation of an internal wave attractor in a confined, stably stratified fluid. *Nature*, 388(6642):557–561, 1997.

[30] W. McLean and W. C. H. McLean. *Strongly Elliptic Systems and Boundary Integral Equations*. Cambridge University Press, 2000.

[31] I. Nikolaev and E. Zhuzhoma. *Flows on 2-dimensional Manifolds: An Overview*. Lecture Notes in Mathematics. Springer Berlin Heidelberg, 2006.

[32] G. I. Ogilvie. Wave attractors and the asymptotic dissipation rate of tidal disturbances. *J. Fluid Mech.*, 543:19–44, 2005.

[33] D. E. Pelinovsky. *Localization in Periodic Potentials: From Schrödinger Operators to the Gross–Pitaevskii Equation*. London Mathematical Society Lecture Note Series. Cambridge University Press, 2011.

[34] G. Pillet, T. Dauxois, E. V. Ermanyuk, L. R. M. Maas, and I. N. Sibgatullin. Internal wave attractors in three-dimensional geometries: Trapping by oblique reflection. *J. Fluid Mech.*, 845:203–225, 2018.

[35] J. V. Ralston. On stationary modes in inviscid rotating fluids. *J. Math. Anal. Appl.*, 44(2):366–383, 1973.

[36] M. Rieutord, B. Georgeot, and L. Valdettaro. Inertial waves in a rotating spherical shell: attractors and asymptotic spectrum. *J. Fluid Mech.*, 435:103, 2001.

[37] M. Ruzhansky and V. Turunen. *Pseudo-Differential Operators and Symmetries*. Birkhauser, Berlin, 2010.

[38] M. D. Ryser, N. Nigam, and P. F. Tupper. On the well-posedness of the stochastic allen–cahn equation in two dimensions. *J. Comput. Phys.*, 231(6):2537–2550, 2012.

[39] M. Shub. Morse-Smale systems. *Scholarpedia*, 2(3):1785, 2007. Revision #132702.

[40] S. Smale. Morse inequalities for a dynamical system. *B. Am. Math. Soc.*, 66(1):43–49, 1960.

[41] S. H. Strogatz. *Nonlinear dynamics and chaos with student solutions manual: With applications to physics, biology, chemistry, and engineering*. CRC press, 2018.

[42] Z. Tao. 0-th Order Pseudo-differential Operator on the Circle. *arXiv e-prints*, page arXiv:1909.06316, September 2019.

[43] L. N. Trefethen. *Spectral Methods in MATLAB*. Society for Industrial and Applied Mathematics, Philadelphia, PA, 2000.

[44] J. Wang. Dynamics of resonances for 0th order pseudodifferential operators. *arXiv e-prints*, page arXiv:2006.11951, June 2020.

# Appendix A

# Morse-Smale Flow

The following content has been extracted from [12, 21, 31]. In what follows, $M$ is a finite-dimensional, smooth, compact manifold and $f^t : M \to M$ will denote a standard $C^k$-flow ($k \geq 0$) for $t \in \mathbb{R}$.

**Definition A.1** (Equilibrium points, periodic orbits)**.** *A point $x_0 \in M$ is an equilibrium (or critical point) of the flow $f^t$ if $f^t(x_0) = x_0$ for all $t \in \mathbb{R}^+$. An orbit $\Gamma \subset M$ is a periodic orbit of minimal period $\tau$ if $\Gamma = \{r(t), t \in \mathbb{R}\}$ where $r(t+\tau) = r(t)$ for $t \in \mathbb{R}^+$ and $r(t+s) \neq r(t)$ for any $s \in (0, \tau) \cap \mathbb{R}^+$.*

**Definition A.2** (Stable/unstable set of a point)**.** *Let $x_0 \in M$ be an equilibrium point. The stable set $W^s(x_0)$ (resp. the unstable set $W^u(x_0)$) of $x_0$ is the set of all initial values $x \in M$ such that $f^t(x) \to x_0$ as $t \to +\infty$ (resp. as $t \to -\infty$).*

**Definition A.3** (Hyperbolicity of a point)**.** *Let $Df^1(x_0)$ be the linear operator given by the derivative of $f^t(x)$ with respect to $x$ evaluated at $t = 1$, $x = x_0$. The point $x_0 \in M$ is hyperbolic if the spectrum of $Df^1(x_0)$ is bounded away from the unit circle with center zero in the complex plane.*

**Remark A.4.** *If $x_0$ is hyperbolic, then there is a neighbourhood $U$ of $x_0$ such that $W^s(x_0) \cap U$ and $W^u(x_0) \cap U$ are $C^k$-manifolds whenever $f^t$ is a $C^k$-flow.*

**Definition A.5** (Stable/unstable set of a periodic orbit)**.** *Let $\Gamma = \{r(t), t \in \mathbb{R}\}$, $r(t) = f^t(r(0))$, $t \in \mathbb{R}$ be a periodic orbit of minimal period $\tau$. The stable and unstable sets of a periodic orbit $\Gamma$ are defined respectively as:*

$$W^s(\Gamma) := \Big\{x \in M : \lim_{t \to +\infty} \mathrm{dist}_M(f^t(x), \Gamma) = 0\Big\},$$
$$W^u(\Gamma) := \Big\{x \in M : \lim_{t \to -\infty} \mathrm{dist}_M(f^t(x), \Gamma) = 0\Big\}.$$

**Definition A.6** (Hyperbolicity of a periodic orbit)**.** *Let $\Gamma = \{r(t), t \in \mathbb{R}\}$ be a periodic orbit of minimal period $\tau$. Assume that $\Gamma$ is a $C^1$-manifold. Let $\Sigma$ be a transversal to the curve $\Gamma$ at a fixed (but arbitrary) point $r_0$. Consider a neighbourhood $U$ in $\Sigma$ of $r_0$ such that, for any $x \in U$, there is a continuous function $\alpha = \alpha(x)$, $\alpha(r_0) = \tau$ such that $\widetilde{f}(x) := f^{\alpha(x)}(x) \in \Sigma$ ($\widetilde{f}$ is known as the Poincaré map on the transversal $\Sigma$). The periodic orbit $\Gamma$ is said to*

*be hyperbolic if the Poincaré map $\widetilde{f}$ is a $C^1$-function and if the spectrum of $D\widetilde{f}(r_0)$ (cf. Definition A.3) has no element of modulus one.*

**Definition A.7** (Morse-Smale flow)**.** *A flow $f^t$ is called a "Morse-Smale flow" if the following properties hold:*

1. *There are only a finite number of equilibria, each one of them hyperbolic with smooth stable and unstable manifolds.*
2. *There are only a finite number of periodic orbits, each of them hyperbolic with smooth stable and unstable manifolds.*
3. *Stable and unstable manifolds of equilibria and periodic orbits intersect transversally, that is, for any $x \in W^u(\Lambda_1) \cap W^s(\Lambda_2)$ (with $\Lambda_1$, $\Lambda_2$ being either an equilibrium point or a periodic orbit), there holds*

$$T_x M = T_x W^u(\Lambda_1) + T_x W^s(\Lambda_2),$$

   *where $T_x M$ denotes the tangent space of $M$ at $x$.*

4. *The union of equilibria and periodic orbits coincides with the non-wandering set $\Omega(f)$, defined as*

$$\Omega(f) := \Big\{ x \in M : \forall \text{ neighbourhood } V \text{ of } x,\ \forall\, t_0 \in \mathbb{R}^+, \\ \exists\, t \in \mathbb{R}^+ \cap (t_0, +\infty) \text{ with } f^t(V) \cap V \neq \emptyset \Big\}.$$

# Appendix B

# MATLAB® Codes

The numerical experiments presented in this work have been performed on a standard computer with 16 GB of RAM, using MATLAB® as a programming language. In this chapter, we compile the main functions developed for these purposes. The complete repository will be available at

github.com/javieralmonacid/internal-waves

after this thesis has been submitted to the SFU Library.

## B.1 Runge-Kutta RK4 solver

```
function [UF,KX,KY,tsteps] = rk4fft2(P,beta,r,omega0,N,dt,T,fun,u0,snaps)
% RK4FFT2 RK4–FFT2 based transient solver
%   RK4FFT2(P,beta,r,omega0,N,dt,T,fun,u0,snaps) returns the solution
%   to the problem in the 2–torus
%
%       i u_t – (P(x,y,D) + r*beta(x,y))* u = fun(x,y)*exp(–i*omega0*t),
%       u = u0 at initial time.
%
%   The time discretization is based on the classical fourth–order
%   Runge–Kutta method. In turn, the space pseudo–spectral discretization
%   uses the built–in function FFT2.
%
%   Input arguments:
%       P (function handle): symbol of the pseudo–differential operator P,
%           for example, P = @(kx,ky) ky./sqrt(1+kx.^2+ky.^2).
%       beta (function handle): boundary–like smooth periodic function.
%       r (float, nonnegative): parameter related to the roughness of the
%           solution. The higher the value, the more singular is.
%       omega0 (float): forcing frequency.
%       N (int): number of gridpoints in the periodic interval [–pi,pi]
```

```
%       dt (float, positive): time step.
%       T (float, positive): final time of simulation.
%       fun (function handle): complex forcing function in real space.
%       u0 (function handle / N-by-N matrix): Initial data.
%       snaps (int, nonzero): snapshots of the evolution between time 0
%           and time T, equally spaced if (T/snaps)/dt is an integer value.
%
%   Returns:
%       UF (N-by-N-by-(snaps+1) array): Solution in Fourier Space to the IVP
%           at times 0,...,T. UF(:,:,k) returns a 2D array corresponding to
%           the solution at the k-th snapshot. The solution at initial and
%           final times is always included.
%       KX, KY (N-by-N array): 2D wavenumbers in the default order by Matlab.
%       tsteps (1-by-N array): recorded times.
%
%   Added to v1.3: u0 can also be a N-by-N matrix.
%
%   See also FFT2 IFFT2 ETDRK4FFT2 MAKEITPERIODIC
%
%   Author: Javier Almonacid
%           Department of Mathematics
%           Simon Fraser University
%   Date:   2020/05/06 (v1.4)

x = 2*pi*(-N/2:N/2-1)'/N; y = x;
ky = [0:N/2-1 -N/2 -N/2+1:-1]'; kx = ky;
[X,Y] = meshgrid(x,y); [KX,KY] = meshgrid(kx,ky);
F = fft2(fun(X,Y));
LIN = -1i*P(KX,KY);
CX = beta(X,Y);

if r == 0
    NON = @(vv,tt) -1i*F.*exp(-1i*omega0*tt);
else
    NON = @(vv,tt) 1i*r*fft2(CX.*ifft2(vv)) - 1i*F.*exp(-1i*omega0*tt);
end

if isa(u0,'function_handle')
    U = fft2(u0(X,Y));
else
    U = fft2(u0);
end

nmax = round(T/dt); nplt = floor((T/snaps)/dt);

UF = U; tsteps = 0;

```

```
for n = 1:nmax
    t = (n-1)*dt;
    k1 = dt*(LIN.*U + NON(U,t));
    k2 = dt*(LIN.*(U+k1/2) + NON(U+k1/2,t+dt/2));
    k3 = dt*(LIN.*(U+k2/2) + NON(U+k2/2,t+dt/2));
    k4 = dt*(LIN.*(U+k3) + NON(U+k3,t+dt));
    U = U + (k1 + 2*k2 + 2*k3 + k4)/6;
    if mod(n,nplt)==0
        UF = cat(3,UF,U);
        tsteps = cat(1,tsteps,n*dt);
    end
end

% This is in case the endtime was not recorded.
if mod(nmax,nplt) ~= 0
    UF = cat(3,UF,U);
    tsteps = cat(1,tsteps,t);
end

tsteps = tsteps';
```

## B.2 Exponential time differencing ETDRK4 solver

```
function [UF,KX,KY,tsteps] = etdrk4fft2(P,beta,r,omega0,N,dt,T,fun,u0,snaps)
% ETDRK4FFT2 ETDRK4-FFT2 based transient solver
%   ETDRK4FFT2(P,beta,r,omega0,N,dt,T,fun,u0,snaps) returns the solution
%   to the problem in the 2-torus
%
%       i u_t - (P(x,y,D) + r*beta(x,y))* u = fun(x,y)*exp(-i*omega0*t),
%       u = u0 at initial time.
%
%   The time discretization is based on the Exponential Time-Differencing
%   Runge-Kutta 4-th order (ETDRK4) from Kassam & Trefethen (2005). In turn,
%   the space pseudo-spectral discretization uses the built-in function FFT2.
%
%   Input arguments:
%       P (function handle): symbol of the pseudo-differential operator P,
%           for example, P = @(kx,ky) ky./sqrt(1+kx.^2+ky.^2).
%       beta (function handle): boundary-like smooth periodic function.
%       r (float, nonnegative): parameter related to the roughness of the
%           solution. The higher the value, the more singular is.
%       omega0 (float): forcing frequency.
%       N (int): number of gridpoints in the periodic interval [-pi,pi]
%       dt (float, positive): time step.
%       T (float, positive): final time of simulation.
```

```
%       fun (function handle): complex forcing function in real space.
%       u0 (function handle / N-by-N matrix): Initial data.
%       snaps (int, nonzero): snapshots of the evolution between time 0
%           and time T, equally spaced if (T/snaps)/dt is an integer value.
%
%   Returns:
%       UF (N-by-N-by-(snaps+1) array): Solution in Fourier Space to the IVP
%           at times 0,...,T. UF(:,:,k) returns a 2D array corresponding to
%           the solution at the k-th snapshot. The solution at initial and
%           final times is always included.
%       KX, KY (N-by-N array): 2D wavenumbers in the default order by Matlab.
%       tsteps (1-by-N array): recorded times.
%
%   Added to v1.3: u0 can also be a N-by-N matrix.
%
%   See also FFT2 IFFT2 RK4FFT2 MAKEITPERIODIC
%
%   Author: Javier Almonacid
%           Department of Mathematics
%           Simon Fraser University
%   Date:   2020/05/06 (v1.4)

ky = [0:N/2-1 -N/2 -N/2+1:-1]'; kx = ky;
[KX,KY] = meshgrid(kx,ky);
LIN = -1i*P(KX,KY);
clear kx ky;

% ETDRK4 quantities
E = exp(dt*LIN); E2 = exp(dt*LIN/2);
M = 64; % Number of discretization points in the circle
LIN = reshape(LIN,N^2,1);
rts = exp(2*(1:M)*pi*1i/M); % Roots of unity
LR = dt*LIN(:,ones(M,1)) + rts(ones(N^2,1),:); % MOST EXPENSIVE PART
clear LIN rts;
Q     = dt*mean( (exp(LR/2)-1)./LR ,2);  % Trapezoidal rule
alpha = dt*mean( (-4-LR+exp(LR).*(4-3*LR+LR.^2))./LR.^3 ,2);
breta = dt*mean( (2+LR+exp(LR).*(-2+LR))./LR.^3 ,2);
gamma = dt*mean( (-4-3*LR-LR.^2+exp(LR).*(4-LR))./LR.^3 ,2);
clear LR;
Q = reshape(Q,N,N); alpha = reshape(alpha,N,N);
breta = reshape(breta,N,N); gamma = reshape(gamma,N,N);

x = 2*pi*(-N/2:N/2-1)'/N; y = x;
[X,Y] = meshgrid(x,y);
F = fft2(fun(X,Y));
CX = beta(X,Y);
if r == 0
```

```
    NON = @(vv,tt) -1i*F.*exp(-1i*omega0*tt);
else
    NON = @(vv,tt) 1i*r*fft2(CX.*ifft2(vv)) - 1i*F.*exp(-1i*omega0*tt);
end

if isa(u0,'function_handle')
    U = fft2(u0(X,Y));
else
    U = fft2(u0);
end

% Time-stepping loop
nmax = round(T/dt); nplt = floor((T/snaps)/dt);

UF = U; tsteps = 0;

for n = 1:nmax
    t = (n-1)*dt;
    NU = NON(U,t);
    A = E2.*U + Q.*NU;
    NA = NON(A,t+dt/2);
    B = E2.*U + Q.*NA;
    NB = NON(B,t+dt/2);
    C = E2.*A + Q.*(2*NB-NU);
    NC = NON(C,t+dt);
    U = E.*U + alpha.*NU + 2*breta.*(NA+NB) + gamma.*NC;
    if mod(n,nplt)==0
        UF = cat(3,UF,U);
        tsteps = cat(1,tsteps,n*dt);
    end
end

% This is in case the endtime was not recorded.
if mod(nmax,nplt) ~= 0
    UF = cat(3,UF,U);
    tsteps = cat(1,tsteps,t);
end

tsteps = tsteps';
```

## B.3 Discretization of the pseudo-differential operator

```
function H = matrix_construction_full(PM,BM,r)
% MATRIX_CONSTRUCTION_FULL Matrix for eigenvalue problem.
%       MATRIX_CONSTRUCTION_FULL(PM,BM,r) returns the discretization
%               matrix corresponding to the operator
%                               P(D) - r*beta(x)
%               where \Delta is the standard Laplacian in the 2-torus.
%
%       Input arguments:
%               PM (2D array): Evaluation of the symbol p(\xi) in the
%                       2D wavenumbers, e.g., PM = p(KX,KY).
%               BM (2D array): Evaluation of the function beta in the
%                       2D X, Y coordinates, i.e., BM = beta(X,Y).
%               r (float): roughness parameter.
%
%       Returns
%               H (2D matrix, full): If PM and BM are of size N-by-N, then
%                       H is N^2-by-N^2 full matrix.
%
%       See also: eigensolver
%
%   Author: Javier Almonacid
%           Department of Mathematics
%           Simon Fraser University
%   Date:   2020/05/18 (v1.0)
%
N = size(PM,2);

% Diagonal parts
PM = PM(:);
BM = BM(:);

% Final matrix
H = fft(eye(N));
H = kron(H,H);
H = diag(PM)-r*H*diag(BM)*H'/N^2;
```

## B.4 Eigenvalue and eigenvector solver

```
function [lambda,VF,KX,KY] = eigensolver(r,beta,nu,N,eigvals)
% EIGENSOLVER Eigenvalue solver
%   EIGENSOLVER(r,beta,nu,N,eigvals) computes the first 'eigvals'
%   of the operator
%
%           <D>^{-1} D_y + 1i*nu*\Delta - r*beta
%
%   using a pseudo-spectral method by means of a DFT with N modes per
%   direction. If eigvals << N^2, then the algorithm the built-in function
%   "eigs". If eigvals is not provided, or eigvals = N^2, then it uses "eig".
%
%   Input arguments:
%       r (float): roughness parameter,
%       beta (function handle): beta function in the defintion of
%           the operator.
%       nu (float, nonegative): viscosity.
%       N (int): discretization points on the periodic interval [-pi,pi].
%       eigvals (int, <= N^2): amount of eigenvalues to compute.
%
%   Returns:
%       lambda (eigvals-by-1 array): eigenvalues of the operator.
%           They are ordered in ascending order of magnitude, with
%           eigenvalues with positive real part appearing first,
%           then those with negative real part. If nu = 0, the eigenvalues
%           are real, so they are ordered in ascending order.
%       VF (N-by-N-by-eigvals array): eigenfunctions in Fourier space
%           (unshifted). VF(:,:,k) is the eigenfunction corresponding to the
%           k-th eigenvalue.
%       KX, KY (N-by-N array): 2D wavenumbers in the default order by Matlab.
%
%   See also ETDRK4FFT2 RK4FFT2 MAKEITPERIODIC EIGS
%
%   Author: Javier Almonacid
%           Department of Mathematics
%           Simon Fraser University
%   Date:   2020/05/18 (v1.1)

% Matrix construction
P = @(kx,ky) ky./sqrt(1+kx.^2+ky.^2) - 1i*nu*(kx.^2+ky.^2);
x = 2*pi*(-N/2:N/2-1)'/N; y = x;
[X,Y] = meshgrid(x,y);
BM = beta(X,Y);

ky = [0:N/2-1 -N/2 -N/2+1:-1]'; kx = ky;
[KX,KY] = meshgrid(kx,ky);
```

```
PM = P(KX,KY);

F2 = matrix_construction_full(PM,BM,r);

% Eigenvalue solver
if nargin > 4
    F2 = sparse(F2); % To be able to use 'eigs' instead of 'eig'
    try
        [VF,lambda] = eigs(F2,[],eigvals,0,'Display',1);
    catch ME
        if strcmp(ME.identifier,'MATLAB:eigs:SingularA')
            % 0 is a eigenvalue, replacing initial shift by nearby value
            warning('Matrix is singular. Replacing shift by 1e-10i')
            [VF,lambda] = eigs(F2,[],eigvals,1e-10i);
        end
    end
else
    % If eigvals is not provided, compute all using 'eig'
    warning(['Computing ALL ',num2str(N^2),' eigenvalues for nu = ',num2str(
        nu)])
    [VF,lambda] = eig(F2);
end
lambda = diag(lambda);

% Sort eigenfunctions
if nu ~= 0
    % OLD ORDER
    % Sorted in increasing order of magnitude then phase
    %[lambda,ii] = sort(lambda);
    % NEW ORDER
    % Positive real part first, then negative real part
    pos = find(real(lambda)>=0);
    neg = setdiff(1:length(lambda),pos)';
    ii = [pos; neg];
    lambda = lambda(ii);
else
    % Spectrum appears to be continuous with no imaginary part.
    [lambda,ii] = sort(lambda,'ComparisonMethod','real');
end
VF = VF(:,ii);

% Reshape into 2D arrays and IFFT
VF = reshape(VF,N,N,length(lambda));
```

## B.5 Radial energy density

```
function [R,G] = red(s,UF,KX,KY)
% RED s-level Radial Energy Density (RED)
%       RED(s,UF,KX,KY) returns the decay of the shell-summed Fourier
%       coefficients.
%
%       Input arguments:
%               s (float): level of the RED
%               UF (3D array): time-dependent grid function at times given
%           in the third coordinate.
%               KX, KY (2D array): 2D wavenumbers in the default order by
%           Matlab.
%
%       Returns:
%               G (2D array): Radial energy density at each time. If UF is
%           of size N-by-N-by-M, then G is an M-by-(N/4) array, with
%           each row correspoding to a different time, and each column
%           to a different R.
%               R (1D array): Radius for the RED between R and N/2. The
    annulus
%           has width equal to 2, so R is a 1-by-N/4 array.
%
%       See also RK4FFT2 ETDRK4FFT2
%
%   Author: Javier Almonacid
%           Department of Mathematics
%           Simon Fraser University
%   Date:   2020/05/13 (v1.1)


for l =1:size(UF,3)
    % Shift everything so wavenumber (0,0) is at the center of the spectrum.
    UF(:,:,l) = fftshift(UF(:,:,l));
end
KX = fftshift(KX); KY = fftshift(KY);

N = size(UF,1);
KX = KX(:); KY = KY(:);
m = sqrt(KX.^2 + KY.^2);
R = 2:2:N/2;
G = zeros(size(UF,3),N/4);

for l = 1:length(R)
    jin = find( (R(l)-2 <= m) & (m < R(l)) ); % Find all values R-2<= m <R
    % Find associated wavenumbers
    pos = [KX(jin),KY(jin)]+N/2+1; % Shift to coincide with Matlab indexing
```

```
    elem = sub2ind([N N],pos(:,2),pos(:,1));
    for row = 1:size(UF,3)
        Uaux = UF(:,:,row);
        G(row,l) = sum((1+KX(jin).^2+KY(jin).^2).^s.*abs(Uaux(elem)).^2)/N^2;
    end
end
```

## B.6 Discrete Sobolev norm

```
function snorm = hsnorm(UF,KX,KY,s)
% HSNORM H^s Sobolev norm.
%       HSNORM(UF,KX,KY,s) returns the H^s discrete Sobolev norm of UF.
%
%       Input arguments:
%               UF (2D array): Grid function in Fourier space.
%               KX, KY (2D array): 2D wavenumbers in the default order by
%                       Matlab.
%               s (float): s power in the definition of the norm.
%
%       Returns:
%               snorm (float): H^s norm of UF.
%
%       See also RED NORM
%
%   Author: Javier Almonacid
%           Department of Mathematics
%           Simon Fraser University
%   Date:   2020/05/13 (v1.0)

N = size(UF,2);
UF = UF(:); KX = KX(:); KY = KY(:);

snorm = (1+KX.^2+KY.^2).^s.*abs(UF).^2;
snorm = (4*pi^2/N^4)*sum(snorm);
snorm = sqrt(snorm);
```

## B.7 Transformation from frequency to real space

```
function [U,X,Y] = fourier2real(UF)
% FOURIER2REAL Convert a grid function in Fourier space into Real space.
%       FOURIER2REAL(UF) returns a time-dependent grid function in Real space
%
%       Input arguments:
```

```
%               UF (3D array): time-dependent grid function in Fourier space.
%                       The time is stored in the third coordinate.
%
%       Returns:
%               U (3D array): time-dependent grid function in Real space.
%                       At the k-th time, the code computes ifft2(UF(:,:,k)).
%               X, Y (2D array): X, Y coordinates.
%
%       See also: RK4FFT2 ETDRK4FFT2 EIGENSOLVER
%
%   Author: Javier Almonacid
%           Department of Mathematics
%           Simon Fraser University
%   Date:   2020/05/13 (v1.0)

N = size(UF,1); % Get grid points in each direction
x = 2*pi*(-N/2:N/2-1)'/N;
[X,Y] = meshgrid(x,x);
U = zeros(size(UF));

L = size(UF,3);
for k = 1:L
    U(:,:,k) = ifft2(UF(:,:,k));        % IFFT2 at each time
end
```

## B.8 Extension of a grid function to the whole period

```
function [UU,XX,YY] = makeitperiodic(U,X,Y)
% MAKEITPERIODIC Patch a grid function to make it visibly periodic.
%       MAKEITPERIODIC(U,X,Y) adds an extra column and row to U,X,Y,
%               to make U truly periodic. If U is in Fourier space, then this
%               function shifts the (0,0) wavenumberto the center of the
%               spectrum. This is useful, in particular, when plotting in
%               Real or Fourier space.
%
%       Input arguments:
%               U (3D array): time-dependent grid function. The time is
%                       stored in the third coordinate.
%               X, Y (2D array): If U is in Real space, then these are
%                       the X, Y coordinates. If U is in Fourier space, then
%                       these are the KX, KY 2D wavenumbers in the default
%                       order by Matlab.
%
%       Returns:
%               UU (3D array): If U is of size N-by-N-by-M, then UU is
```

```
%                       of size (N+1)-by-(N+1)-by-M containing the missing
%                       entries that make U a visibly periodic function.
%                       If U is in Fourier space, then UU is shifted so that
%                       the wavenumber (0,0) appears in the center of the
%                       spectrum.
%               XX, YY (2D array): If X, Y are of size N-by-N, then XX, YY
%                       are of size (N+1)-by-(N+1). If X, Y are coordinates
%                       in real space, then XX, YY is a meshgrid-type pair
%                       that contains, in addition to the components of X and
%                       Y, the coordinate x=pi and y=pi. If X, Y are integer
%                       wavenumbers then XX, YY contains also the wavenumber
%                       kx = N/2 and ky = N/2.
%
%       See also RK4FFT2 ETDRK4FFT2 EIGENSOLVER
%
%   Author: Javier Almonacid
%           Department of Mathematics
%           Simon Fraser University
%   Date:   2020/05/12 (v1.0)

N = size(X,1);

if X(1,1) == 0  % Input is in Fourier space
    X = fftshift(X);    Y = fftshift(Y);
    for l = 1:size(U,3)
        U(:,:,l) = fftshift(U(:,:,l));
    end
end

c = -X(1,1);
XX = [X, c*ones(N,1); X(1,:), c];
YY = [Y, Y(:,1); c*ones(1,N), c];
UU = zeros(size(U)+[1 1 0]);
for l = 1:size(U,3)
    UU(:,:,l) = [U(:,:,l), U(:,1,l); U(1,:,l), U(1,1,l)];
end
```